

## Magnetotellurics: the CBB or phase tensor and Bahr's 1988 analysis

Frederick E. M. Lilley

To cite this article: Frederick E. M. Lilley (2020): Magnetotellurics: the CBB or phase tensor and Bahr's 1988 analysis, Exploration Geophysics, DOI: [10.1080/08123985.2020.1717333](https://doi.org/10.1080/08123985.2020.1717333)

To link to this article: <https://doi.org/10.1080/08123985.2020.1717333>



© 2020 The Author(s). Published by Informa UK Limited, trading as Taylor & Francis Group

---



Published online: 13 May 2020.

---



Submit your article to this journal [↗](#)

---



Article views: 197

---



View related articles [↗](#)


---



View Crossmark data [↗](#)

---

# Magnetotellurics: the CBB or phase tensor and Bahr's 1988 analysis

Frederick E. M. Lilley 

Research School of Earth Sciences, Australian National University, Canberra, ACT, Australia

## ABSTRACT

The phase tensor of magnetotellurics is analysed in terms of its invariants with regard to axes rotation. These invariants are displayed as conic sections (ellipses), eigenvectors, and as Mohr diagrams. Attention is drawn to a supplementary ellipse which may be constructed to complement the usual phase tensor ellipse. The two ellipses together help convey the full information available from phase tensor analysis. For the cases of 1D and 2D regional structure, the ellipses, eigenvectors and Mohr diagrams show distinctive features, such as no preferred strike direction in the case of 1D, and a consistent strike (or across-strike) direction in the case of 2D. In the general case of 3D regional structure a "closest 2D strike" direction may be apparent, though there is a range of possibilities for this quantity. The range includes Bahr's regional strike estimates, which are shown to be given by the eigenvectors of the phase tensor. Generally in this paper, the phase tensor will be referred to as the CBB tensor, in recognition of its discoverers Caldwell, Bibby and Brown.

## ARTICLE HISTORY

Received 21 May 2019  
Accepted 6 September 2019

## KEYWORDS

Decomposition;  
electromagnetism;  
geomagnetism; geophysics;  
magnetotellurics; tensor

## 1. Introduction

Contemporary magnetotelluric (MT) practice commonly involves the use of three tensors: the distortion tensor which may be modelled, often numerically, to assist in interpretation; the basic MT tensor which relates observed magnetic and electric fields; and the "phase tensor" which is not observed directly but is calculated from the MT tensor.

This paper is intended as an introduction to the phase tensor and follows earlier papers (Lilley, 2016, 2018) which introduced, in turn, the distortion tensor and the MT tensor. See also Lilley and Phillips (2018) for a description of the distortion tensor. In addition to being well-described in texts on magnetotellurics such as Chave and Jones (2012), the phase tensor has also been recently reviewed by Booker (2014). This paper is intended to be both complementary and supplementary to these works.

As there is much activity in MT in Australia at present, for example, Roberston et al. (2017), with new practitioners involved, the present manuscript will emphasise the basic linear algebra aspects of phase tensor analysis with a worked numerical example. An ellipse supplementary to that commonly used to depict phase tensors will be introduced, and Mohr diagrams will also be used to illustrate phase tensor properties. Direct eigenanalysis of the phase tensor, and its link to the earlier work of Bahr (1988), will be included.

It should at the outset be emphasised that "phase tensor" may be a misleading name, especially for

newcomers to the subject. In the context of the field practice of magnetotellurics, where an MT tensor relates two vector quantities both of which are observed, there may be an expectation that a "phase tensor" will be based on actual field observations of phase. However, the elements of phase tensors are derived from calculated MT tensors, are not themselves observed, and are not observed phase angles in any sense.

Indeed it is important to emphasise that the elements of the phase tensor are not phase angles. Under particular circumstances only, they are the tangent values of some very particular phase angles.

Such confusion is avoided in the present paper where, in recognition of its discoverers Caldwell, Bibby and Brown, the phase tensor is generally referred to as the CBB tensor.

## 2. The CBB tensor

Caldwell, Bibby, and Brown (2004) introduced the CBB tensor as calculated from an observed MT tensor, and the concept was further developed by Bibby, Caldwell, and Brown (2005). Taking the MT equation as

$$\mathbf{E} = \mathbf{ZH} \quad (1)$$

where  $\mathbf{E}$  and  $\mathbf{H}$  denote the electric and magnetic fields, all quantities are complex functions of frequency, and  $\mathbf{Z}$  is the MT tensor with in-phase and quadrature parts  $\mathbf{Z}_p$

and  $\mathbf{Z}_q$  such that

$$\mathbf{Z} = \mathbf{Z}_p + i\mathbf{Z}_q \quad (2)$$

and other quantities similarly, then the CBB tensor is a real matrix defined as

$$\Phi = \mathbf{Z}_p^{-1}\mathbf{Z}_q \quad (3)$$

by Caldwell, Bibby, and Brown (2004) who use for it the notation  $\Phi$ .

Henceforth in this paper, however, to avoid confusion with the common usage of  $\Phi$  and  $\phi$  as actual angles of phase, the notation  $\mathbf{A}$  will be used for the CBB tensor in place of  $\Phi$ . Then

$$\mathbf{A} = \mathbf{Z}_p^{-1}\mathbf{Z}_q \quad (4)$$

For MT observations which are assumed to be affected by local galvanic distortion of the electric field according to

$$\mathbf{Z} = \mathbf{D}\mathbf{Z}^b \quad (5)$$

where  $\mathbf{D}$  is a pure real distortion matrix and  $\mathbf{Z}^b$  is the MT tensor before distortion, then

$$\mathbf{Z}_p = \mathbf{D}\mathbf{Z}_p^b \quad (6)$$

and

$$\mathbf{Z}_q = \mathbf{D}\mathbf{Z}_q^b \quad (7)$$

From Equation (4)

$$\mathbf{Z}_p\mathbf{A} = \mathbf{Z}_q \quad (8)$$

and substituting from Equations (6) and (7) gives

$$\mathbf{D}\mathbf{Z}_p^b\mathbf{A} = \mathbf{D}\mathbf{Z}_q^b \quad (9)$$

and so

$$\mathbf{A} = [\mathbf{Z}_p^b]^{-1}\mathbf{Z}_q^b \quad (10)$$

for non-singular  $\mathbf{D}$  (and a naturally occurring  $\mathbf{D}$  is most unlikely to be exactly singular).

The CBB tensor as calculated by Equation (4) is thus a  $2 \times 2$  matrix, free of galvanic distortion as defined. It is a measure of the process of EM induction in the Earth and, to the extent that it is possible to do so with an inversion process, CBB tensor data contribute to quantitative information on Earth conductivity structure (Tietze, Ritter, and Egbert, 2015). Such inversion processes are complicated, for the CBB matrix is a non-linear function of the MT tensor components used to compute it, and these components are in turn non-linear functions of the parameters describing the regional Earth conductivity structure (Kelbert et al., 2014). The inversion of CBB matrix data is a major frontier of contemporary MT practice (Avdeeva et al., 2015).

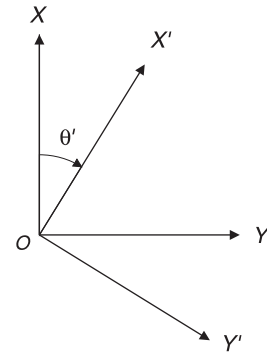


**Figure 1.** The rotation of axes by angle  $\theta'$ , from  $OX$  and  $OY$  (north and east) to  $OX'$  and  $OY'$ .

### 3. Rotation of observing axes

Short of inverting or interpreting the CBB matrix as calculated, present common usage of it involves axes rotation. The purpose of the axes rotation is to bring out in the data some characteristic which indicates that, for some particular rotation angle, the axes are now aligned along and across geologic strike. Such axes rotation will now be described quite generally.

Taking horizontal directions north and east and denoting them by  $OX$  and  $OY$  respectively with  $OZ$  vertically downwards, upon rotation by angle  $\theta'$  as shown in Figure 1 the axes will be denoted  $OX'$  and  $OY'$ .

First introduce a rotation matrix  $\mathbf{R}(\theta)$  as

$$\mathbf{R}(\theta) = \begin{bmatrix} \cos \theta & \sin \theta \\ -\sin \theta & \cos \theta \end{bmatrix} \quad (11)$$

Then to get a context for how the values of the CBB matrix change when the observing axes of the original MT tensor are rotated, note that the basic MT tensor  $\mathbf{Z}$  changes according to the following: relative to new axes rotated through angle  $\theta'$  as in Figure 1, the electric and magnetic fields  $\mathbf{E}'$  and  $\mathbf{H}'$  will be related to  $\mathbf{E}$  and  $\mathbf{H}$  by

$$\mathbf{E}' = \mathbf{R}(\theta')\mathbf{E} \quad (12)$$

and

$$\mathbf{H}' = \mathbf{R}(\theta')\mathbf{H} \quad (13)$$

so that

$$\mathbf{E} = \mathbf{R}(-\theta')\mathbf{E}' \quad (14)$$

and

$$\mathbf{H} = \mathbf{R}(-\theta')\mathbf{H}' \quad (15)$$

and substituting Equations (14) and (15) into Equation (1) gives

$$\mathbf{R}(-\theta')\mathbf{E}' = \mathbf{Z}\mathbf{R}(-\theta')\mathbf{H}' \quad (16)$$

Thus denoting by  $\mathbf{Z}'$  the MT tensor as would be observed in the rotated axes, Equation (1) becomes

$$\mathbf{E}' = \mathbf{Z}'\mathbf{H}' \quad (17)$$

with  $\mathbf{Z}$  and  $\mathbf{Z}'$  related by

$$\mathbf{Z}' = \mathbf{R}(\theta')\mathbf{Z}\mathbf{R}(-\theta') \quad (18)$$

and so also by

$$\mathbf{Z} = \mathbf{R}(-\theta')\mathbf{Z}'\mathbf{R}(\theta') \quad (19)$$

Note that because  $\mathbf{R}(\theta)$  is a pure real matrix, Equation (18) can be expressed in its in-phase and out-of-phase parts as

$$\mathbf{Z}'_p = \mathbf{R}(\theta')\mathbf{Z}_p\mathbf{R}(-\theta') \quad (20)$$

and

$$\mathbf{Z}'_q = \mathbf{R}(\theta')\mathbf{Z}_q\mathbf{R}(-\theta') \quad (21)$$

or equivalently

$$\mathbf{Z}_p = \mathbf{R}(-\theta')\mathbf{Z}'_p\mathbf{R}(\theta') \quad (22)$$

and

$$\mathbf{Z}_q = \mathbf{R}(-\theta')\mathbf{Z}'_q\mathbf{R}(\theta') \quad (23)$$

From Equation (22) an expression for  $[\mathbf{Z}_p]^{-1}$ , needed for Equation (4), may now be obtained as

$$\mathbf{Z}_p^{-1} = [\mathbf{R}(-\theta')\mathbf{Z}'_p\mathbf{R}(\theta')]^{-1} \quad (24)$$

Remembering from Frazer, Duncan, and Collar (1963, 25) that if  $\mathbf{S} = \mathbf{UVW}$  for matrices  $\mathbf{S}$ ,  $\mathbf{U}$ ,  $\mathbf{V}$  and  $\mathbf{W}$  then  $\mathbf{S}^{-1} = \mathbf{W}^{-1}\mathbf{V}^{-1}\mathbf{U}^{-1}$ , the inverse  $\mathbf{Z}_p^{-1}$  may be expressed

$$\mathbf{Z}_p^{-1} = [\mathbf{R}(\theta')]^{-1}[\mathbf{Z}'_p]^{-1}[\mathbf{R}(-\theta')]^{-1} \quad (25)$$

Equation (25) may now be combined with Equation (23) to give, for Equation (4),

$$\mathbf{A} = [\mathbf{R}(\theta')]^{-1}[\mathbf{Z}'_p]^{-1}\mathbf{Z}'_q\mathbf{R}(\theta') \quad (26)$$

and so, because  $[\mathbf{R}(\theta')]^{-1} = \mathbf{R}(-\theta')$ ,

$$\mathbf{A} = \mathbf{R}(-\theta')[\mathbf{Z}'_p]^{-1}\mathbf{Z}'_q\mathbf{R}(\theta') \quad (27)$$

Further, defining  $\mathbf{A}'$  as

$$\mathbf{A}' = [\mathbf{Z}'_p]^{-1}\mathbf{Z}'_q \quad (28)$$

then

$$\mathbf{A}' = \mathbf{R}(\theta')\mathbf{A}\mathbf{R}(-\theta') \quad (29)$$

The similar forms of Equations (18) and (29) show that when observing axes are rotated, the CBB tensor changes in just the same way as does the MT tensor from which it is calculated, though it is a non-linear function of the latter.

### 3.1. The CBB tensor under rotation of axes

Denoting the elements of  $\mathbf{Z}_p$  as  $[Z_{xxp}, Z_{xyp}, Z_{yxq}, Z_{yyq}]$  and of  $\mathbf{Z}_q$  as  $[Z_{xxq}, Z_{xyq}, Z_{yxq}, Z_{yyq}]$  the CBB tensor as defined by Equation (4) is

$$\mathbf{A} = \frac{1}{\det \mathbf{Z}_p} \begin{bmatrix} Z_{yyq} & -Z_{xyp} \\ -Z_{yxq} & Z_{xxp} \end{bmatrix} \begin{bmatrix} Z_{xxq} & Z_{xyq} \\ Z_{yxq} & Z_{yyq} \end{bmatrix} \quad (30)$$

which may be expanded to give

$$\mathbf{A} = \frac{1}{Z_{xxp}Z_{yyq} - Z_{xyp}Z_{yxq}} \times \begin{bmatrix} Z_{yyq}Z_{xxq} - Z_{xyp}Z_{yxq} & Z_{yyq}Z_{xyq} - Z_{xyp}Z_{yyq} \\ -Z_{yxq}Z_{xxq} + Z_{xxp}Z_{yxq} & -Z_{yxq}Z_{xyq} + Z_{xxp}Z_{yyq} \end{bmatrix} \quad (31)$$

and under rotation of axes

$$\mathbf{A}' = \frac{1}{Z'_{xxp}Z'_{yyq} - Z'_{xyp}Z'_{yxq}} \times \begin{bmatrix} Z'_{yyq}Z'_{xxq} - Z'_{xyp}Z'_{yxq} & Z'_{yyq}Z'_{xyq} - Z'_{xyp}Z'_{yyq} \\ -Z'_{yxq}Z'_{xxq} + Z'_{xxp}Z'_{yxq} & -Z'_{yxq}Z'_{xyq} + Z'_{xxp}Z'_{yyq} \end{bmatrix} \quad (32)$$

For 2D structures, when the observing axes are aligned either along or across the geologic strike, basic electromagnetic theory gives the result that  $\mathbf{Z}'_p$  and  $\mathbf{Z}'_q$  take the form  $[0, Z'_{xyp}, Z'_{yxq}, 0]$  and  $[0, Z'_{xyq}, Z'_{yxq}, 0]$ . The quantities  $(Z'_{xyp} + iZ'_{yxq})$  and  $(Z'_{xyq} + iZ'_{yxq})$  are then known as the E-pol and B-pol impedances or vice-versa (and sometimes as the TE and TM impedances).

The CBB tensor  $\mathbf{A}'$  then takes the form

$$\mathbf{A}' = \begin{bmatrix} Z'_{yxq}/Z'_{yxq} & 0 \\ 0 & Z'_{xyq}/Z'_{xyq} \end{bmatrix} \quad (33)$$

which is seen to be diagonal, with the  $A'_{xx}$  and  $A'_{yy}$  elements taking the values of the tangents of the along and across-strike phase angles, which for 2D situations are defined as  $\arctan(Z'_{xyq}/Z'_{yxq})$  and  $\arctan(Z'_{yxq}/Z'_{yxq})$ .

It is the search for such a 2D geologic strike direction, in the present instance revealed by the rotated CBB tensor showing a diagonal form, which drives not only the present CBB method but also, quite generally, methods such as that of Bahr (1988) which seek a direction for regional geologic strike.

Also quite generally, when observed data do not conform to the 2D ideal for some particular rotation direction, "closest" or in some sense "best fitting" 2D strike directions may be sought, according to certain criteria.

However, on the basis of single-station horizontal-field MT data alone, there is always an ambiguity in a determination of geologic strike, which may be either along strike or across strike.

## 4. The CBB matrix as a fictitious operator and its representation by two ellipses

### 4.1. The first ellipse

The CBB matrix does not actually operate on any measurable quantity to give another measurable quantity, but it is implicitly imagined to do so by Caldwell, Bibby, and Brown (2004, 469) and Bibby, Caldwell, and Brown (2005, 930); and also by Weidelt and Chave (2012, 135) and Booker (2014). Such hypothetical models provide a geographic reference frame for the geometric representation of the CBB matrix by an ellipse.

Thus imagining that some vector quantity  $\mathbf{V}$  is related to another vector quantity  $\mathbf{v}$  by

$$\mathbf{V} = \mathbf{A}\mathbf{v} \quad (34)$$

it is then possible to represent a number of the characteristics of this equation (and so of matrix  $\mathbf{A}$ ) by conic sections, and in particular by ellipses. This point is demonstrated generally, for example, by Nye (1957), and for MT in particular by Lilley (1976). Nye refers to the figures as representation quadrics, with radial arms of a particular length and in a particular direction. Note however that Nye (and Lilley) are dealing with measurable (not imagined) quantities as, in his earlier work, is Bibby (1986).

Now further imagine that Equation (34) applies in the same geographic space and relative to the same measurement axes as Equation (1). That is,

$$\begin{bmatrix} V_x \\ V_y \end{bmatrix} = \begin{bmatrix} A_{xx} & A_{xy} \\ A_{yx} & A_{yy} \end{bmatrix} \begin{bmatrix} v_x \\ v_y \end{bmatrix} \quad (35)$$

and take, as a numeric example,  $\mathbf{A} = [2.44, 1.61; 0.50, 1.20]$  to give

$$\begin{bmatrix} V_x \\ V_y \end{bmatrix} = \begin{bmatrix} 2.44 & 1.61 \\ 0.50 & 1.20 \end{bmatrix} \begin{bmatrix} v_x \\ v_y \end{bmatrix} \quad (36)$$

where the source of this numeric example is given in Section 13 below.

Then consider a  $\mathbf{V}$  signal of amplitude  $V$  and bearing  $\theta$  to accompany a  $\mathbf{v}$  signal of amplitude  $v$  and bearing  $\phi$ . Equation (35) becomes

$$\begin{bmatrix} V \cos \theta \\ V \sin \theta \end{bmatrix} = \begin{bmatrix} A_{xx} & A_{xy} \\ A_{yx} & A_{yy} \end{bmatrix} \begin{bmatrix} v \cos \phi \\ v \sin \phi \end{bmatrix} \quad (37)$$

which gives

$$V^2 = v^2 [(A_{xx}^2 + A_{yx}^2) \cos^2 \phi + (A_{xy}^2 + A_{yy}^2) \sin^2 \phi + (A_{xx}A_{xy} + A_{yx}A_{yy}) \sin 2\phi] \quad (38)$$

Then if say  $\phi$  is varied through  $2\pi$  while the amplitude of  $\mathbf{v}$  is adjusted so that the amplitude of  $\mathbf{V}$  is maintained at unity,  $v_x = v \cos \phi$ ,  $v_y = v \sin \phi$  and Equation (38)

becomes

$$(A_{xx}^2 + A_{yx}^2)v_x^2 + (A_{xy}^2 + A_{yy}^2)v_y^2 + 2(A_{xx}A_{xy} + A_{yx}A_{yy})v_xv_y = 1 \quad (39)$$

which may be expressed

$$[v_x \ v_y] \mathbf{A}^T \mathbf{A} \begin{bmatrix} v_x \\ v_y \end{bmatrix} = 1 \quad (40)$$

and is the familiar equation for an ellipse when  $v_x$  and  $v_y$  are plotted appropriately. It can be seen that Equation (39) has the form

$$ax^2 + 2bxy + cy^2 = 1 \quad (41)$$

where  $a = (A_{xx}^2 + A_{yx}^2)$ ,  $b = (A_{xx}A_{xy} + A_{yx}A_{yy})$  and  $c = (A_{xy}^2 + A_{yy}^2)$ . For the current example,  $a = 6.20$ ,  $b = 4.53$  and  $c = 4.03$ .

Equation (39) may thus be expressed

$$[v_x \ v_y] \begin{bmatrix} a & b \\ b & c \end{bmatrix} \begin{bmatrix} v_x \\ v_y \end{bmatrix} = 1 \quad (42)$$

and, for the example,

$$[v_x \ v_y] \begin{bmatrix} 6.20 & 4.53 \\ 4.53 & 4.03 \end{bmatrix} \begin{bmatrix} v_x \\ v_y \end{bmatrix} = 1 \quad (43)$$

Note that the matrix in Equation (42) is symmetric, as is the numerical example in Equation (43); whereas the matrix in Equation (35) in general is not symmetric (just as the numerical example in Equation (36) is not symmetric).

In Equation (42) the matrix  $[a, b; b, c]$ , being symmetric, may be diagonalised by eigenanalysis to give

$$[v_x \ v_y] \begin{bmatrix} Q_{xx} & Q_{xy} \\ Q_{yx} & Q_{yy} \end{bmatrix} \begin{bmatrix} \lambda_1 & 0 \\ 0 & \lambda_2 \end{bmatrix} \begin{bmatrix} Q_{xx} & Q_{yx} \\ Q_{xy} & Q_{yy} \end{bmatrix} \begin{bmatrix} v_x \\ v_y \end{bmatrix} = 1 \quad (44)$$

where  $\lambda_1$  and  $\lambda_2$  are the eigenvalues of  $[a, b; b, c]$  and the orthonormal eigenvectors (of unit length and perpendicular to each other) are  $[Q_{xx} \ Q_{yx}]^T$  for  $\lambda_1$  and  $[Q_{xy} \ Q_{yy}]^T$  for  $\lambda_2$ .

For the example,

$$[v_x \ v_y] \begin{bmatrix} 0.785 & -0.619 \\ 0.619 & 0.785 \end{bmatrix} \begin{bmatrix} 9.78 & 0 \\ 0 & 0.461 \end{bmatrix} \begin{bmatrix} 0.785 & 0.619 \\ -0.619 & 0.785 \end{bmatrix} \begin{bmatrix} v_x \\ v_y \end{bmatrix} = 1 \quad (45)$$

so that  $\lambda_1 = 9.78$  with  $[Q_{xx} \ Q_{yx}]^T = [0.785 \ 0.619]^T$ , and  $\lambda_2 = 0.461$  with  $[Q_{xy} \ Q_{yy}]^T = [-0.619 \ 0.785]^T$ .

The ellipse then has semi-axes of magnitude  $\lambda_1^{-1/2}$  ( $= 0.320$ ) and  $\lambda_2^{-1/2}$  ( $= 1.47$ ). The directions of the ellipse axes are those of the eigenvectors, at rotations  $\arctan(Q_{yx}/Q_{xx})$  ( $= 38.3^\circ$ ) and  $\arctan(Q_{yy}/Q_{xy})$  ( $=$

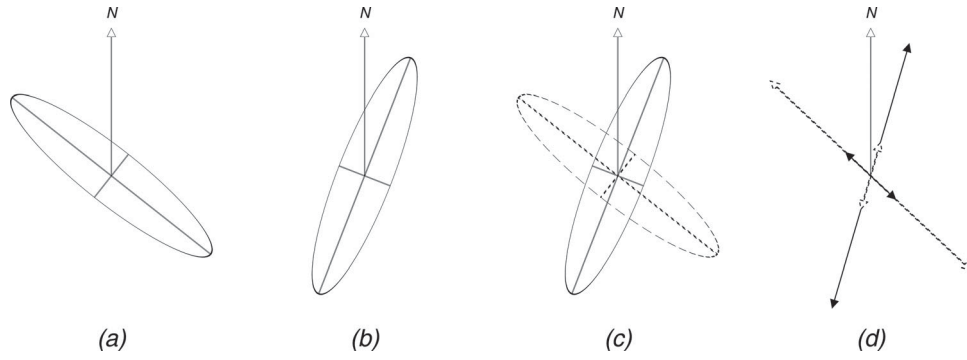


**Figure 2.** Three ellipse diagrams for the example matrix [2.44, 1.61; 0.50, 1.20], and a fourth diagram for its eigenvectors. North (bearing zero) is to the top of the figure. (a) The first ellipse derived in this paper. The major axis is at bearing  $-51.7^\circ$  and the minor axis is at bearing  $38.3^\circ$ . (b) The second ellipse derived in this paper, and the traditional CBB ellipse. The major axis is at bearing  $21.3^\circ$  and the minor axis is at bearing  $-68.7^\circ$ . (c) The two ellipses plotted together, with the first ellipse dashed. The two major axes fail orthogonality by  $17.0^\circ$ , which CBB refers to as the “skew” angle. (d) The results of eigenanalysis of the example matrix (solid lines) and of the inverse of that matrix (dashed lines), see Section 6 below. The eigenvectors also fail orthogonality, by  $26.9^\circ$ . In this figure, all ellipses are drawn with the same major axis length. Thus regarding axis length, only the ratio of the major and minor axis lengths is significant. Note that for  $\mathbf{V} = \mathbf{A}\mathbf{v}$  with  $\mathbf{V}$  and  $\mathbf{v}$  as polar vectors,  $\mathbf{v}$  describing the ellipse in (a) results in  $\mathbf{V}$  describing a circle; and  $\mathbf{v}$  describing a circle results in  $\mathbf{V}$  describing the ellipse in (b).

$-51.7^\circ$ ) from the original  $XOY$  (and  $v_x O v_y$ ) axes, as can be seen by writing Equation (44) as

$$\begin{bmatrix} v'_x & v'_y \end{bmatrix} \begin{bmatrix} \lambda_1 & 0 \\ 0 & \lambda_2 \end{bmatrix} \begin{bmatrix} v'_x \\ v'_y \end{bmatrix} = 1 \quad (46)$$

where  $v'_x = v_x \cos \tau + v_y \sin \tau$  and  $v'_y = -v_x \sin \tau + v_y \cos \tau$  with  $\tau = 38.3^\circ$ , that is

$$\lambda_1 v'^2_x + \lambda_2 v'^2_y = 1 \quad (47)$$

This ellipse is shown in Figure 2(a).

#### 4.2. The second ellipse

Given the hypothetical nature of Equation (34), it is equally valid to consider a second figure, drawn by a radial arm proportional to  $\mathbf{V}$  and plotted at bearing  $\theta$  with the magnitude of  $\mathbf{v}$  maintained at unity. Equation (34) is written as

$$\mathbf{v} = \mathbf{A}^{-1}\mathbf{V} \quad (48)$$

where,  $\mathbf{A}$  being invertible, its inverse is given by

$$\mathbf{A}^{-1} = \frac{1}{\det \mathbf{A}} \begin{bmatrix} A_{yy} & -A_{xy} \\ -A_{yx} & A_{xx} \end{bmatrix} \quad (49)$$

Equation (37) then becomes

$$\begin{bmatrix} v \cos \phi \\ v \sin \phi \end{bmatrix} = \frac{1}{\det \mathbf{A}} \begin{bmatrix} A_{yy} & -A_{xy} \\ -A_{yx} & A_{xx} \end{bmatrix} \begin{bmatrix} V \cos \theta \\ V \sin \theta \end{bmatrix} \quad (50)$$

and

$$\begin{bmatrix} v \cos \phi \\ v \sin \phi \end{bmatrix} = \frac{1}{2.123} \begin{bmatrix} 1.20 & -1.61 \\ -0.50 & 2.44 \end{bmatrix} \begin{bmatrix} V \cos \theta \\ V \sin \theta \end{bmatrix} \quad (51)$$

in the current example.

Equation (38) becomes

$$v^2(\det \mathbf{A})^2 = V^2[(A_{yy}^2 + A_{yx}^2) \cos^2 \theta + (A_{xy}^2 + A_{xx}^2) \sin^2 \theta - (A_{yy}A_{xy} + A_{yx}A_{xx}) \sin 2\theta] \quad (52)$$

and if now  $\mathbf{v}$  is maintained at unit amplitude and the amplitude of  $\mathbf{V}$  is plotted at angle  $\theta$  as  $\theta$  is varied through  $2\pi$ , remembering  $V_x = V \cos \theta$  and  $V_y = V \sin \theta$  the equation is given

$$(A_{yy}^2 + A_{yx}^2)V_x^2 + (A_{xy}^2 + A_{xx}^2)V_y^2 - 2(A_{yy}A_{xy} + A_{yx}A_{xx})V_xV_y = (\det \mathbf{A})^2 \quad (53)$$

Equation (53) may again be expressed in the form of Equation (42)

$$\begin{bmatrix} V_x & V_y \end{bmatrix} \begin{bmatrix} a & b \\ b & c \end{bmatrix} \begin{bmatrix} V_x \\ V_y \end{bmatrix} = 1 \quad (54)$$

but now  $a = (A_{yy}^2 + A_{yx}^2)/(\det \mathbf{A})^2$ ,  $b = -(A_{yy}A_{xy} + A_{yx}A_{xx})/(\det \mathbf{A})^2$  and  $c = (A_{xy}^2 + A_{xx}^2)/(\det \mathbf{A})^2$ . For the current example,  $a = 0.375$ ,  $b = -0.699$ ,  $c = 1.90$  and eigenanalysis as before now gives

$$\begin{bmatrix} V_x & V_y \end{bmatrix} \begin{bmatrix} 0.363 & 0.931 \\ -0.931 & 0.363 \end{bmatrix} \begin{bmatrix} 2.17 & 0 \\ 0 & 0.102 \end{bmatrix} \times \begin{bmatrix} 0.363 & -0.931 \\ 0.931 & 0.363 \end{bmatrix} \begin{bmatrix} V_x \\ V_y \end{bmatrix} = 1 \quad (55)$$

Thus again the equivalent of Equation (46) is reached as

$$\begin{bmatrix} v'_x & v'_y \end{bmatrix} \begin{bmatrix} \lambda_1 & 0 \\ 0 & \lambda_2 \end{bmatrix} \begin{bmatrix} v'_x \\ v'_y \end{bmatrix} = 1 \quad (56)$$

but with different eigenvalues and eigenvectors than before.

Now for the numerical example,  $\lambda_1 = 2.17$  with  $[Q_{xx} \ Q_{yx}]^T = [0.363 \ -0.931]^T$ , and  $\lambda_2 = 0.102$  with

$[Q_{xy} \ Q_{yy}]^T = [0.931 \ 0.363]^T$ . The ellipse then has semi-axes of magnitude  $\lambda_1^{-1/2}$  ( $= 0.679$ ) and  $\lambda_2^{-1/2}$  ( $= 3.13$ ). The directions of the ellipse axes are those of the eigenvectors, at rotations  $\arctan(Q_{yx}/Q_{xx})$  ( $= -68.7^\circ$ ) and  $\arctan(Q_{yy}/Q_{xy})$  ( $= 21.3^\circ$ ) from the original  $XOY$  (and  $V_x \ O \ V_y$ ) axes. This ellipse is shown in Figure 2(b).

Note however that though the eigenvalues are different, they are in the same ratio as before (for the example,  $9.78/0.461 = 21.2$  and  $2.17/0.102 = 21.2$ ). The two ellipses thus have the same shape but are oriented differently, as their eigenvectors are different. Thus generally the same ellipse is given, but at a different rotation angle, as can be seen by comparing Figure 2(a,b).

The procedure set by Caldwell, Bibby, and Brown (2004), which produces Figure 2(b), is generally followed by practitioners. However realising that another ellipse can be drawn, generally at a different orientation as in Figure 2(a), should help emphasise the nature of phase tensor interpretations. Thus Figure 2 explores in (c) a further possible representation of the CBB matrix on a map. Plotting both ellipses demonstrates quantitatively (by any evident lack of their orthogonality) the departure of the CBB matrix from 2-dimensionality. Presenting both ellipses also helps emphasise, especially in the case of 2D data, the ambiguity of the geologic strike which can be in the direction of either the major axis or the minor axis of a CBB ellipse. Without both ellipses plotted, there may be a tendency for the viewer to take a “default” (but unjustified) view that it is always the major axis of a single plotted ellipse which shows the strike direction.

### 4.3. Note on Weidelt and Chave (2012)

Note that  $\mathbf{A}^{-1}$  is not the “alternative definition of the phase tensor” mentioned by Weidelt and Chave (2012, 134). In the notation of the present paper, the alternative phase tensor of Weidelt and Chave (2012) would be  $\mathbf{Z}_q \mathbf{Z}_p^{-1}$ . In contrast,  $\mathbf{A}^{-1}$  as investigated above is  $[\mathbf{Z}_p^{-1} \mathbf{Z}_q]^{-1}$ , that is  $\mathbf{Z}_q^{-1} \mathbf{Z}_p$ .

## 5. The singular value decomposition of the CBB matrix

The singular value decomposition (SVD) of a matrix is one of the most powerful and basic tools of linear algebra. Applying it to the  $2 \times 2$  CBB matrix produces the diagonalisation

$$\begin{bmatrix} A_{xx} & A_{xy} \\ A_{yx} & A_{yy} \end{bmatrix} = \mathbf{R}(\theta_1) \begin{bmatrix} w_1 & 0 \\ 0 & w_2 \end{bmatrix} \mathbf{R}^T(\theta_2) \quad (57)$$

Upon expanding Equation (57), the four individual equations for  $A_{xx}$ ,  $A_{xy}$ ,  $A_{yx}$  and  $A_{yy}$  obtained may be solved to give the following solutions for  $\theta_1$ ,  $\theta_2$ ,  $w_1$  and

$w_2$ :

$$\theta_1 + \theta_2 = \arctan \left[ \frac{A_{xy} + A_{yx}}{A_{yy} - A_{xx}} \right] \quad (58)$$

$$\theta_1 - \theta_2 = \arctan \left[ \frac{A_{xy} - A_{yx}}{A_{xx} + A_{yy}} \right] \quad (59)$$

$$w_1 + w_2 = (A_{xx} - A_{yy}) \sin(\theta_1 - \theta_2) + (A_{xx} + A_{yy}) \cos(\theta_1 - \theta_2) \quad (60)$$

and

$$w_1 - w_2 = (A_{xx} - A_{yy}) \cos(\theta_1 + \theta_2) - (A_{xy} + A_{yx}) \sin(\theta_1 + \theta_2) \quad (61)$$

For the example matrix  $[2.44, 1.61; 0.50, 1.20]$  the above equations give  $\theta_1 = -21.3^\circ$ ,  $\theta_2 = -38.3^\circ$ ,  $w_1 = 3.13$  and  $w_2 = 0.679$ .

Also more formally, see Strang (2006, 331), in Equation (57) the columns of  $\mathbf{R}(\theta_1)$  will be the (orthonormal) eigenvectors of  $\mathbf{A}\mathbf{A}^T$ . The columns of  $\mathbf{R}(\theta_2)$ , and thus the rows of  $\mathbf{R}^T(\theta_2)$ , will be the (orthonormal) eigenvectors of  $\mathbf{A}^T\mathbf{A}$ . The diagonal entries  $w_1$  and  $w_2$  are the singular values of  $\mathbf{A}$ , and are also the square roots of the eigenvalues of both  $\mathbf{A}\mathbf{A}^T$  and  $\mathbf{A}^T\mathbf{A}$ .

For the example the eigenvectors of  $\mathbf{A}\mathbf{A}^T$  are  $[0.932, 0.363]^T$  and  $[-0.363, 0.932]^T$ , while the eigenvectors of  $\mathbf{A}^T\mathbf{A}$  are  $[0.785, 0.619]^T$  and  $[-0.619, 0.785]^T$ . For both cases, the eigenvalues are 9.78 and 0.461 so that the singular values  $w_1$  and  $w_2$  will be 3.13 and 0.679 respectively.

Thus for the example, Equation (57) becomes

$$\begin{bmatrix} A_{xx} & A_{xy} \\ A_{yx} & A_{yy} \end{bmatrix} = \begin{bmatrix} 0.932 & -0.363 \\ 0.363 & 0.932 \end{bmatrix} \begin{bmatrix} 3.13 & 0 \\ 0 & 0.679 \end{bmatrix} \times \begin{bmatrix} 0.785 & 0.619 \\ -0.619 & 0.785 \end{bmatrix} \quad (62)$$

which can be written

$$\begin{bmatrix} A_{xx} & A_{xy} \\ A_{yx} & A_{yy} \end{bmatrix} = \mathbf{R}(-21.3^\circ) \begin{bmatrix} 3.13 & 0 \\ 0 & 0.679 \end{bmatrix} \mathbf{R}^T(-38.3^\circ) \quad (63)$$

Substituting Equation (57) into Equation (35) gives

$$\begin{bmatrix} V_x \\ V_y \end{bmatrix} = \mathbf{R}(\theta_1) \begin{bmatrix} w_1 & 0 \\ 0 & w_2 \end{bmatrix} \mathbf{R}^T(\theta_2) \begin{bmatrix} V'_x \\ V'_y \end{bmatrix} \quad (64)$$

Thus

$$\mathbf{R}(-\theta_1) \begin{bmatrix} V_x \\ V_y \end{bmatrix} = \begin{bmatrix} w_1 & 0 \\ 0 & w_2 \end{bmatrix} \mathbf{R}(\theta_1 - \theta_2) \mathbf{R}(-\theta_1) \begin{bmatrix} V'_x \\ V'_y \end{bmatrix} \quad (65)$$

and so

$$\begin{bmatrix} V'_x \\ V'_y \end{bmatrix} = \begin{bmatrix} w_1 & 0 \\ 0 & w_2 \end{bmatrix} \mathbf{R}(\theta_1 - \theta_2) \begin{bmatrix} V'_x \\ V'_y \end{bmatrix} \quad (66)$$

where  $V'_x$ ,  $V'_y$ ,  $v'_x$  and  $v'_y$  are the components of  $\mathbf{V}$  and  $\mathbf{v}$  in a coordinate system rotated angle  $-\theta_1$ , that is

$\begin{bmatrix} V'_x \\ V'_y \end{bmatrix} = \mathbf{R}(-\theta_1) \begin{bmatrix} V_x \\ V_y \end{bmatrix}$  and  $\begin{bmatrix} v'_x \\ v'_y \end{bmatrix} = \mathbf{R}(-\theta_1) \begin{bmatrix} v_x \\ v_y \end{bmatrix}$ , following the form of Equation (12).

In Equation (66) if  $v$  is kept at unit amplitude and allowed to vary in direction  $\phi$  in the rotated axes, then  $\begin{bmatrix} v'_x \\ v'_y \end{bmatrix} = \begin{bmatrix} \cos \phi \\ \sin \phi \end{bmatrix}$  and Equation (66) becomes

$$\begin{bmatrix} V'_x \\ V'_y \end{bmatrix} = \begin{bmatrix} w_1 & 0 \\ 0 & w_2 \end{bmatrix} \mathbf{R}(\theta_1 - \theta_2) \begin{bmatrix} \cos \phi \\ \sin \phi \end{bmatrix} \quad (67)$$

Remembering that  $\sin^2(\phi - \theta_1 + \theta_2) + \cos^2(\phi - \theta_1 + \theta_2) = 1$  the equation of an ellipse is reached

$$\frac{V'^2_x}{w_1^2} + \frac{V'^2_y}{w_2^2} = 1 \quad (68)$$

where the major axis of the ellipse will be aligned with the rotated  $V'_x$  axis, i.e. at bearing  $-\theta_1$  to the original direction of north.

For the example,  $\theta_1 = -21.3^\circ$ ,  $w_1 = 3.13$  and  $w_2 = 0.679$ . The ellipse is the second ellipse of Section 4.2, and is depicted in Figure 2(b).

If however in Equation (64) the axes are rotated by angle  $\theta_2$ , and a  $\mathbf{V}$  of unit amplitude is considered to occur at a varying direction  $\theta$  in the rotated axes, then now  $\begin{bmatrix} V'_x \\ V'_y \end{bmatrix} = \begin{bmatrix} \cos \theta \\ \sin \theta \end{bmatrix}$  and in place of Equation (67) we have

$$\mathbf{R}(-\theta_1 + \theta_2) \begin{bmatrix} \cos \theta \\ \sin \theta \end{bmatrix} = \begin{bmatrix} w_1 & 0 \\ 0 & w_2 \end{bmatrix} \begin{bmatrix} V'_x \\ V'_y \end{bmatrix} \quad (69)$$

leading to the ellipse equation

$$\frac{V'^2_x}{(1/w_1)^2} + \frac{V'^2_y}{(1/w_2)^2} = 1 \quad (70)$$

This ellipse will have its minor axis in the direction of  $-\theta_2$ . For the example,  $\theta_2 = -38.3^\circ$ , and the ellipse is that depicted in Figure 2(a).

## 6. Eigenanalysis of the CBB matrix

For comparison, the results of the direct eigenanalysis of the matrix [2.44, 1.61; 0.50, 1.20] are also shown in Figure 2(d). As explained in Lilley (2016), in this analysis solutions are sought for the equation which expresses  $\mathbf{V}$  and  $\mathbf{v}$  to be parallel:

$$\mathbf{V} = \zeta \mathbf{v} \quad (71)$$

where  $\zeta$  is a real scalar, and so

$$(\mathbf{A} - \zeta \mathbf{I}) \cdot \mathbf{v} = 0 \quad (72)$$

A direction in which  $\mathbf{V}$  and  $\mathbf{v}$  are parallel is an eigenvector of  $\mathbf{A}$ , and quantity  $\zeta$  is the corresponding eigenvalue.

The example matrix  $\mathbf{A}$  is not symmetric, so the eigenvectors are not orthogonal. However, the eigenvalues

are real and different because

$$(A_{xx} + A_{yy})^2 + 4(A_{xy}A_{yx} - A_{xx}A_{yy}) > 0 \quad (73)$$

and both are positive as the trace ( $\text{tr}\mathbf{A}$ ) and determinant ( $\det\mathbf{A}$ ) of  $\mathbf{A}$  are both positive, having values 3.64 and 2.12 respectively.

The results obtained by standard eigenanalysis (Strang, 2006) are that there is an eigenvalue of 2.91 at bearing  $16.3^\circ$  (or equivalently  $-163.7^\circ$ ) together with an eigenvalue of 0.73 at bearing  $133.2^\circ$  (or equivalently  $-46.8^\circ$ ). These eigenvectors are shown in Figure 2(d) as solid lines.

For  $\mathbf{A}^{-1}$  there is an eigenvalue of 1.37 (the reciprocal of 0.73) at bearing  $133.2^\circ$  (or  $-46.8^\circ$ ), and an eigenvalue of 0.344 (the reciprocal of 2.91) at bearing  $16.3^\circ$  (or  $-163.7^\circ$ ). These eigenvectors for  $\mathbf{A}^{-1}$  are also shown, as dashed lines, in Figure 2(d).

In Figure 2(d) the eigenvectors of  $\mathbf{A}^{-1}$  have been drawn at a scale which gives them the same lengths as the corresponding eigenvectors of  $\mathbf{A}$ , so that the figure does not suggest either to be the more likely strike direction. This convention is followed throughout the present paper when eigenvalues of  $\mathbf{A}$  and  $\mathbf{A}^{-1}$  are presented together.

## 7. Eigenanalysis and Bahr's regional strike estimates

There is a fundamental link between the CBB matrix and the analysis of Bahr (1988) in that direct eigenanalysis of the CBB matrix produces Bahr's regional strike directions. This result may be seen algebraically by taking Equation (31) and again assuming Equation (34). With the rotation of axes Equation (34) becomes

$$\mathbf{V}' = \mathbf{A}' \mathbf{v}' \quad (74)$$

of component equations

$$V'_x = A'_{xx}v'_x + A'_{xy}v'_y \quad (75)$$

and

$$V'_y = A'_{yx}v'_x + A'_{yy}v'_y \quad (76)$$

which expand to

$$V'_x = \frac{1}{Z'_{xxp}Z'_{yyq} - Z'_{xyp}Z'_{yxq}} \left[ (Z'_{yyq}Z'_{xxq} - Z'_{xyp}Z'_{yxq})v'_x + (Z'_{yyq}Z'_{xyq} - Z'_{xyp}Z'_{yyq})v'_y \right] \quad (77)$$

and

$$V'_y = \frac{1}{Z'_{xxp}Z'_{yyq} - Z'_{xyp}Z'_{yxq}} \left[ (-Z'_{yxq}Z'_{xxq} + Z'_{xxp}Z'_{yxq})v'_x + (-Z'_{yxq}Z'_{xyq} + Z'_{xxp}Z'_{yyq})v'_y \right] \quad (78)$$

If a rotation direction is sought for which the resultant  $\mathbf{V}'$  has only a component  $V'_x$  and is parallel to an applied



$\mathbf{v}'$  which has only a component  $v'_x$  (the definition of an eigenvector, see Equation (71)) then the condition is needed that  $V'_y = 0$  for  $v'_y = 0$ , i.e.

$$A'_{yx} = 0 \quad (79)$$

or, expanding  $A'_{yx}$ ,

$$\frac{1}{Z'_{xxp}Z'_{yyq} - Z'_{xyp}Z'_{yxq}} (-Z'_{yxp}Z'_{xxq} + Z'_{xxp}Z'_{yxq}) = 0 \quad (80)$$

For  $Z'_{xxp}Z'_{yyq} - Z'_{xyp}Z'_{yxq} \neq 0$  Equation (80) gives

$$\frac{Z'_{xxp}}{Z'_{xyp}} = \frac{Z'_{xxq}}{Z'_{yxq}} \quad (81)$$

which is exactly the equation of Bahr (1988, 123, eq. 9) by which the regional strike directions of 2D or near-2D MT data are determined. Thus the eigenvectors of the CBB matrix are the two regional strike directions of Bahr. For locally distorted but otherwise regionally 2D MT data, the Bahr directions will be along and across strike. For 3D data, the strike directions will not be orthogonal but may be taken as approximately along and across strike for the data regarded as being approximately 2D regionally.

The equation which Bahr (1988) derives from Equation (81) above is (using  $\mathcal{A}$ ,  $\mathcal{B}$  and  $\mathcal{C}$  for Bahr's  $A$ ,  $B$  and  $C$ )

$$-\mathcal{A} \sin(2\alpha) + \mathcal{B} \cos(2\alpha) + \mathcal{C} = 0 \quad (82)$$

of solutions

$$\tan \alpha_{1,2} = \pm[(\mathcal{B} + \mathcal{C})/(\mathcal{B} - \mathcal{C}) + (\mathcal{A}/(\mathcal{B} - \mathcal{C}))^2]^{1/2} - \mathcal{A}/(\mathcal{B} - \mathcal{C}) \quad (83)$$

In this paper now distinguish these two solutions as

$$\tan \alpha_1 = +[(\mathcal{B} + \mathcal{C})/(\mathcal{B} - \mathcal{C}) + (\mathcal{A}/(\mathcal{B} - \mathcal{C}))^2]^{1/2} - \mathcal{A}/(\mathcal{B} - \mathcal{C}) \quad (84)$$

and

$$\tan \alpha_2 = -[(\mathcal{B} + \mathcal{C})/(\mathcal{B} - \mathcal{C}) + (\mathcal{A}/(\mathcal{B} - \mathcal{C}))^2]^{1/2} - \mathcal{A}/(\mathcal{B} - \mathcal{C}) \quad (85)$$

Returning to Equation (78) above, the eigenvector condition is also met if a rotation direction is sought for which the resultant  $\mathbf{V}'$  has component  $V'_y$  only and is parallel to an applied  $\mathbf{v}'$  which has component  $v'_y$  only. Then the condition is needed that  $V'_x = 0$  for  $v'_x = 0$ , i.e.

$$A'_{xy} = 0 \quad (86)$$

The condition then required is that

$$\frac{Z'_{yyq}}{Z'_{xyp}} = \frac{Z'_{yyq}}{Z'_{xyq}} \quad (87)$$

which in the context of his own analysis is noted by Bahr (1988) but not pursued further there.

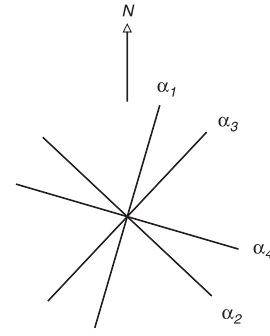


**Figure 3.** The eight possible directions of a rotated  $OX'$  axis as given by the analysis of Bahr (1988) for the CBB matrix [2.44, 1.61; 0.50, 1.20].  $\alpha_1 = 16.3^\circ$ ,  $\alpha_2 = 133.2^\circ$ ,  $\alpha_3 = 43.2^\circ$  and  $\alpha_4 = 106.3^\circ$ . Note that the  $\alpha_1$  and  $\alpha_4$  directions are perpendicular, as are the  $\alpha_3$  and  $\alpha_2$  directions.

However now note that Equation (87) leads to

$$-\mathcal{A} \sin(2\alpha) + \mathcal{B} \cos(2\alpha) - \mathcal{C} = 0 \quad (88)$$

which, differing in the sign of its third term when compared to Equation (82), leads to two further solutions for  $\alpha$ , notably

$$\tan \alpha_3 = +[(\mathcal{B} - \mathcal{C})/(\mathcal{B} + \mathcal{C}) + (\mathcal{A}/(\mathcal{B} + \mathcal{C}))^2]^{1/2} - \mathcal{A}/(\mathcal{B} + \mathcal{C}) \quad (89)$$

and

$$\tan \alpha_4 = -[(\mathcal{B} - \mathcal{C})/(\mathcal{B} + \mathcal{C}) + (\mathcal{A}/(\mathcal{B} + \mathcal{C}))^2]^{1/2} - \mathcal{A}/(\mathcal{B} + \mathcal{C}) \quad (90)$$

Thus the Bahr analysis gives four solutions for  $\alpha$ . They are not however independent; some algebra based on Equations (84) and (90) shows that

$$\tan \alpha_1 \tan \alpha_4 = -1 \quad (91)$$

and thus  $\alpha_4 = \alpha_1 \pm \pi/2$ . Similar application of Equations (85) and (89) shows that

$$\tan \alpha_2 \tan \alpha_3 = -1 \quad (92)$$

and thus  $\alpha_3 = \alpha_2 \pm \pi/2$ .

The four solutions for  $\alpha$  thus give eight possible directions for an  $OX'$  axis, rotated as in Figure 1, to be aligned with a regional geologic strike. For the current example, matrix [2.44, 1.61; 0.50, 1.20], these directions are shown in Figure 3. As expected,  $\alpha_1$  and  $\alpha_2$  can be seen to be the directions of the eigenvectors in Figure 2(d), together with their "cross-directions"  $\alpha_4$  and  $\alpha_3$ .

In the ideal case of 2D regional structure  $\alpha_1 = \alpha_3$ ,  $\alpha_2 = \alpha_4$  and Bahr's  $\mathcal{C} = 0$ . The number of solutions for  $\alpha$  reduces to two at right angles (along and across strike), and the number of possible directions for a rotated  $OX'$  axis reduces to four.

Returning to Figure 2, part (d) is now seen to have an extra significance. It is that the eigenvectors plotted

show the directions of closest 2D strike according to the Bahr (1988) method.

From Equation (75) it can also be seen that the eigenvalue (call it  $\zeta_1$ ) obtained for  $v'_y = 0$  has the value of  $A'_{xx}$  evaluated for the appropriate rotation of axes. Thus

$$\zeta_1 = \frac{Z'_{yy_p} Z'_{xx_q} - Z'_{xy_p} Z'_{yx_q}}{Z'_{xx_p} Z'_{yy_p} - Z'_{xy_p} Z'_{yx_p}} \quad (93)$$

is the coefficient of the linear relationship between  $V'_x$  and  $v'_x$  (with all terms evaluated for the appropriate rotation of axes). For the current example, the angle of rotation of axes is  $16.3^\circ$ , and  $\zeta_1 = 2.91$  (the value of  $A'_{xx}$ ).

Also, from Equation (76) it can be seen that the eigenvalue (call it  $\zeta_2$ ) obtained for  $v'_x = 0$  has the value of  $A'_{yy}$  evaluated for the appropriate rotation of axes. Thus

$$\zeta_2 = \frac{-Z'_{yx_p} Z'_{xy_q} + Z'_{xx_p} Z'_{yy_q}}{Z'_{xx_p} Z'_{yy_p} - Z'_{xy_p} Z'_{yx_p}} \quad (94)$$

is the coefficient of the linear relationship between  $V'_y$  and  $v'_y$  (with all terms evaluated for the appropriate rotation of axes). For the current example, the angle of rotation of axes is  $133.2^\circ$ , and  $\zeta_2 = 0.73$  (the value of  $A'_{yy}$ ).

With reference to Figure 3, the angle  $(\alpha_3 - \alpha_1)$  is an obvious measure of the departure of the data from being 2D. This angle is called  $\gamma$  by Weaver, Agarwal, and Lilley (2003, 2006), and  $\epsilon$  by Lilley (2018). The angle  $(\alpha_1 - \alpha_3)$  is called “ $(\theta_1 - \theta_2)$ ” by Weaver, Agarwal, and Lilley (2000) (in the notation of their paper) where it is also the quantity  $\arcsin l_7$ . Lilley (2018) draws attention to the contrast of Bahr (1988) working with Equations (84) and (85) above, and Weaver, Agarwal, and Lilley (2000) working with Equations (84) and (89) above, so that the “ $(\theta_1 - \theta_2)$ ” values of Weaver, Agarwal, and Lilley (2000) differ by  $90^\circ$  from the  $(\alpha_1 - \alpha_2)$  values of Bahr (1988).

Bahr (1988) himself works with the value of his  $C$  to form various skew parameters, but they do not take the form of angles which can be identified on a diagram like Figure 3.

## 8. Mohr diagram for the CBB matrix

With reference to Equation (29), the matrix  $[A_{xx}, A_{xy}; A_{yx}, A_{yy}]$  upon rotation of axes by angle  $\theta'$  as in Figure 1 changes to  $[A'_{xx}, A'_{xy}; A'_{yx}, A'_{yy}]$  according to

$$\begin{bmatrix} A'_{xx} & A'_{xy} \\ A'_{yx} & A'_{yy} \end{bmatrix} = \mathbf{R}(\theta') \begin{bmatrix} A_{xx} & A_{xy} \\ A_{yx} & A_{yy} \end{bmatrix} \mathbf{R}(-\theta') \quad (95)$$

Expanding Equation (95) shows that the elements of the two matrices  $\mathbf{A}$  and  $\mathbf{A}'$  are related by the equations

$$A'_{xx} = (A_{xx} + A_{yy})/2 + C \sin(2\theta' + \beta) \quad (96)$$

$$A'_{xy} = (A_{xy} - A_{yx})/2 + C \cos(2\theta' + \beta) \quad (97)$$

$$A'_{yx} = -(A_{xy} - A_{yx})/2 + C \cos(2\theta' + \beta) \quad (98)$$

and

$$A'_{yy} = (A_{xx} + A_{yy})/2 - C \sin(2\theta' + \beta) \quad (99)$$

where

$$C = \frac{1}{2}[(A_{xx} - A_{yy})^2 + (A_{xy} + A_{yx})^2]^{1/2} \quad (100)$$

(taking the positive square root) and  $\beta$  is defined by

$$\tan \beta = (A_{xx} - A_{yy})/(A_{xy} + A_{yx}) \quad (101)$$

taking the signs of  $(A_{xx} - A_{yy})$  and  $(A_{xy} + A_{yx})$  into account to give  $\beta$  a range of  $-\pi$  to  $+\pi$ .

It is also useful to define an angle  $\mu$  as

$$\tan \mu = (A_{xy} - A_{yx})/(A_{xx} + A_{yy}) \quad (102)$$

again taking the signs of  $(A_{xy} - A_{yx})$  and  $(A_{xx} + A_{yy})$  into account to give  $\mu$  a range of  $-\pi$  to  $+\pi$ ; and then to define a (positive) quantity  $Z^L$  as

$$Z^L = \frac{1}{2}[(A_{xx} + A_{yy})^2 + (A_{xy} - A_{yx})^2]^{1/2} \quad (103)$$

and further to define an auxiliary angle  $\beta'$  (of range  $-\pi$  to  $+\pi$ ) as

$$\tan \beta' = (A'_{xx} - A'_{yy})/(A'_{xy} + A'_{yx}) \quad (104)$$

Then

$$\theta' = (\beta' - \beta)/2 \quad (105)$$

Note that  $(A'_{xx} + A'_{yy})$ ,  $(A'_{xy} - A'_{yx})$ ,  $C$  and  $Z^L$  are independent of  $\theta'$ , and so are rotational invariants.

It is evident from Equations (96) and 97, squared and added to give

$$[A'_{xx} - (A_{xx} + A_{yy})/2]^2 + [A'_{xy} - (A_{xy} - A_{yx})/2]^2 = C^2 \quad (106)$$

that plotting  $A'_{xx}$  against  $A'_{xy}$  as the axes are rotated as in Figure 1 defines a circle, known (with its axes) as a Mohr diagram. The centre of the circle is at the point  $A'_{xx} = (A_{xx} + A_{yy})/2$ ,  $A'_{xy} = (A_{xy} - A_{yx})/2$  and the radius is  $C$ . The diagram for the current example is shown in Figure 4, with  $C$ ,  $\beta$ ,  $\mu$ ,  $Z^L$ ,  $\beta'$  and  $\theta'$  all marked (the values of the first four are respectively  $1.22$ ,  $30.4^\circ$ ,  $17.0^\circ$  and  $1.90$ ).

Figure 4 also shows angle  $\lambda_A$ , defined by

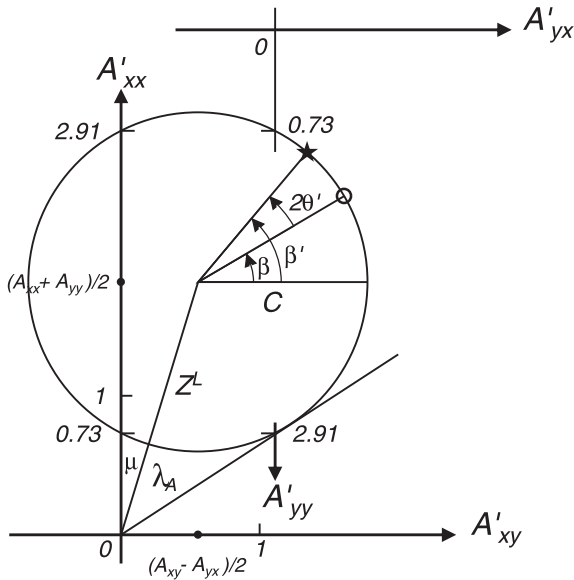
$$\sin \lambda_A = C/Z^L \quad (107)$$

which is a measure of the two-dimensionality of the CBB matrix, and has the value  $40.0^\circ$  for the current example. For 1D data,  $\lambda_A = 0$ .

It is further evident from Equations (98) and (99), squared and added to give

$$[A'_{yy} - (A_{xx} + A_{yy})/2]^2 + [A'_{yx} + (A_{xy} - A_{yx})/2]^2 = C^2 \quad (108)$$

that plotting  $A'_{yy}$  against  $A'_{yx}$  as the axes are rotated also defines a circle. The centre of this circle is at the



- marks initial point
- ★ marks general point after axes rotation by angle  $\theta'$

**Figure 4.** Mohr diagram for the CBB matrix [2.44, 1.61; 0.50, 1.20]. Note that  $\mu$  is reckoned positive clockwise from the vertical axis. The circle crosses the  $A'_{yy}$  axis for  $A'_{yy}$  values of 0.73 and 2.91. The two eigenvector directions are given by the two values of  $\theta'$  which take the general point marked with a star to these  $A'_{yy}$  values of 0.73 and 2.91 respectively. These eigenvector directions are also the Bahr (1988) directions for regional strike (or across strike). The  $A'_{xx}$  values, of the points where the circle crosses the  $A'_{yy}$  axis, are 2.91 and 0.73 respectively. These values are the eigenvalues of the matrix, giving as they do the  $A'_{xx}$  values for the two points on the circle where  $A'_{yx}$  is zero.

point  $A'_{yy} = (A_{xx} + A_{yy})/2$ ,  $A'_{yx} = -(A_{xy} - A_{yx})/2$  and the radius of the circle is again  $C$ . Thus axes for  $A'_{yy}$  and  $A'_{yx}$  can be added to the Mohr diagram for  $A'_{xx}$  and  $A'_{xy}$  as shown in Figure 4. The centre of the circle, at  $A'_{xx} = (A_{xx} + A_{yy})/2$  and  $A'_{yy} = (A_{xx} + A_{yy})/2$  will be halfway between the  $A'_{xy}$  and  $A'_{yx}$  axes. Similarly, because the centre is at  $A'_{xy} = (A_{xy} - A_{yx})/2$  and  $A'_{yx} = -(A_{xy} - A_{yx})/2$  it will be halfway between the  $A'_{xx}$  and  $A'_{yy}$  axes as they are drawn.

On this figure, now with all axes shown, values of  $A'_{xx}$ ,  $A'_{xy}$ ,  $A'_{yx}$  and  $A'_{yy}$  can be read off together for any angle of axes rotation.

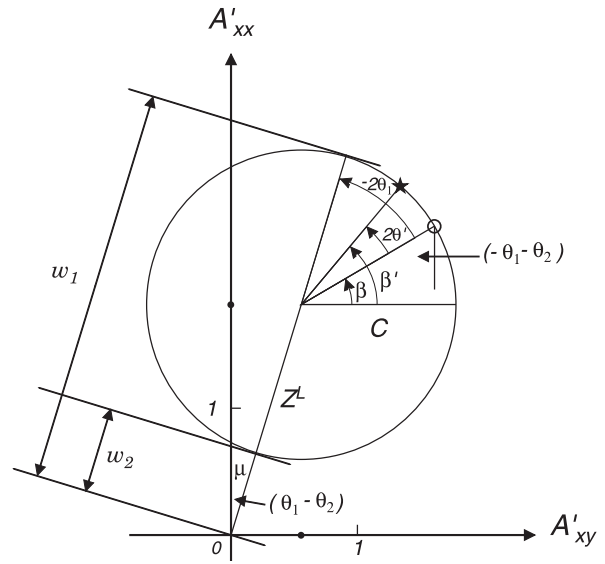
### 8.1. SVD analysis

Now referring back to the SVD analysis, note the connections between  $w_1$ ,  $w_2$ ,  $\theta_1$  and  $\theta_2$  and the Mohr diagram parameters  $C$ ,  $\beta$ ,  $\mu$  and  $Z^L$  to see that the Mohr diagram displays the SVD results  $w_1$  and  $w_2$  as

$$w_1 = Z^L + C \quad (109)$$

and

$$w_2 = Z^L - C \quad (110)$$



- marks initial point
- ★ marks general point after axes rotation by angle  $\theta'$

**Figure 5.** Mohr diagram for the CBB matrix [2.44, 1.61; 0.50, 1.20] as in Figure 4, now with the singular values  $w_1$  (3.13) and  $w_2$  (0.679) shown. Also the angles  $\theta_1$  and  $\theta_2$  from SVD analysis are shown (with  $\theta_1 = -21.3^\circ$  and  $\theta_2 = -38.3^\circ$ , so that  $\theta_1 - \theta_2 = 17.0^\circ$  and  $-\theta_1 - \theta_2 = 59.6^\circ$ ).

and the SVD angles  $\theta_1$  and  $\theta_2$  as

$$\mu = (\theta_1 - \theta_2) \quad (111)$$

and

$$\beta = \pi/2 + (\theta_1 + \theta_2) \quad (112)$$

Then to Figure 4 can be added the SVD values  $w_1$ ,  $w_2$ ,  $\theta_1$  and  $\theta_2$  (respectively 3.13, 0.679,  $-21.3^\circ$  and  $-38.3^\circ$ ) as shown in Figure 5.

### 8.2. Eigenanalysis

The eigenanalysis results are also shown clearly on the Mohr diagram. As discussed in Sections 6 and 7, for a unit  $\mathbf{v}'$  vector in the  $x'$  direction the eigenvector condition is that  $\mathbf{V}'$  shall also be in the  $x'$  direction, so that  $A'_{yx}$  shall be nil as in Equation (79). This latter condition is met at the two points where the circle intersects the  $A'_{yy}$  axis, and is clear for example on the Mohr diagram shown in Figure 4. The directions of the two eigenvectors are thus displayed, as the two values of  $\theta'$  appropriate for the intersection of the circle with the  $A'_{yy}$  axis (at the points marked on the  $A'_{yy}$  axis as 0.73 and 2.91 respectively).

The corresponding eigenvalues, as shown in Section 7, will be the values of  $A'_{xx}$  at those points on the circle where  $A'_{yx}$  is zero. These  $A'_{xx}$  values, of 2.91 and 0.73 respectively, are marked on the  $A'_{xx}$  axis in Figure 4.

Thus the eigenvector for the direction marked  $A'_{yy} = 0.73$  has as its eigenvalue the  $A'_{xx}$  value for  $A'_{yy} = 0.73$ ,

which is  $A'_{xx} = 2.91$ . Similarly the eigenvector for the direction marked  $A'_{yy} = 2.91$  has as its eigenvalue the  $A'_{xx}$  value for  $A'_{yy} = 2.91$ , which is  $A'_{xx} = 0.73$ .

### 8.3. The analysis of Bahr (1988)

In fact a Mohr diagram for the CBB matrix gives a comprehensive depiction of the Bahr (1988) analysis. Some algebra based on the equations of Bahr (1988, 123, above eq. 11) shows that

$$\mathcal{A} = 2(-Z_{xxp}Z_{yyq} + Z_{yyq}Z_{xxq} - Z_{xyq}Z_{yxq} + Z_{yxq}Z_{xyq}) \quad (113)$$

$$\mathcal{B} = 2(Z_{xxp}Z_{yxq} + Z_{yyq}Z_{xyq} - Z_{xyq}Z_{yyq} - Z_{yxq}Z_{xxq}) \quad (114)$$

and

$$\mathcal{C} = 2(Z_{xxp}Z_{yxq} + Z_{xyq}Z_{yyq} - Z_{yxq}Z_{xxq} - Z_{yyq}Z_{xyq}) \quad (115)$$

Reference to Equation (31) shows that Bahr's  $\mathcal{A}$ ,  $\mathcal{B}$  and  $\mathcal{C}$  may thus be expressed

$$\mathcal{A} = 4 \det \mathbf{Z}_p \frac{(A_{xx} - A_{yy})}{2} \quad (116)$$

$$\mathcal{B} = 4 \det \mathbf{Z}_p \frac{(A_{xy} + A_{yx})}{2} \quad (117)$$

and

$$\mathcal{C} = 4 \det \mathbf{Z}_p \frac{(A_{yx} - A_{xy})}{2} \quad (118)$$

Lengths of  $(A_{xx} - A_{yy})/2$ ,  $(A_{xy} + A_{yx})/2$  and  $(A_{yx} - A_{xy})/2$  are evident on a Mohr diagram. Figure 4 is reproduced in Figure 6 with these quantities marked as  $k\mathcal{A}$ ,  $k\mathcal{B}$  and  $k\mathcal{C}$  respectively, where  $k$  denotes the constant  $(4 \det \mathbf{Z}_p)^{-1}$ .

From inspection of Figure 6 the condition for the circle to intersect the  $A'_{xx}$  and  $A'_{yy}$  axes is seen to be

$$\mathcal{A}^2 + \mathcal{B}^2 > \mathcal{C}^2 \quad (119)$$

which is also the condition for real values of  $\alpha$  to be given by the solution of Equation (83).

It is also clear from Figure 6 that when  $\mathcal{C} = 0$ , the Bahr condition for an ideal 2D regional structure, the centre of the circle will move to lie on the  $A'_{xx}$  axis. The two Bahr  $\alpha$  directions are indeed then at right angles, and agree with the SVD results of the CBB analysis for strike direction.

Situations in Figure 6 where the circle just touches the  $A'_{xx}$  and  $A'_{yy}$  axes, or does not intersect them at all, are discussed in a general context in Lilley (2016). In the latter case there are no real eigenvectors, and the method can not be used to give "closest 2D strike". The conclusion to be drawn is that the data are far from approximately 2D.

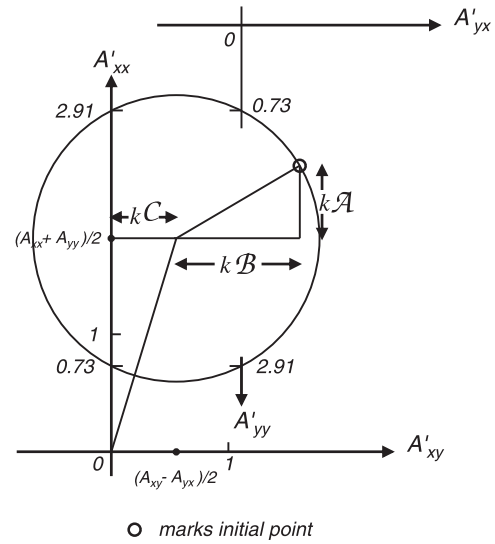


**Figure 6.** Mohr diagram for the CBB matrix [2.44, 1.61; 0.50, 1.20] showing the Bahr  $\mathcal{A}$ ,  $\mathcal{B}$  and  $\mathcal{C}$  quantities marked as  $k\mathcal{A}$ ,  $k\mathcal{B}$  and  $k\mathcal{C}$  where  $k = (4 \det \mathbf{Z}_p)^{-1}$ .

## 9. Use as a "dimensionality tool"

As first advocated by CBB, and employed by many others since, a prime utility of the SVD expression of the CBB matrix lies in its relevance as a "dimensionality tool".

As will be shown below, in a progression from 3D to 2D to 1D regional structures the analysis of the CBB matrix simplifies. Bearing such a progression in mind, the general 3D case is frequently interpreted as giving some indication of its "closest 2D" case (defined in some sense).

Figure 7 combines the SVD ellipses, eigenvectors and Mohr diagram for the current numerical example, and shows how they change if this 3D example is modified first to be 2D, then to be 1D.

### 9.1. The 3D case

Figure 7(a) combines Figure 2(c) and Figure 2(d) with the essential parts of Figure 5. The major axes of the two ellipses depart from orthogonality by the angle  $\mu$  ( $= 17^\circ$ ), which can be seen in the Mohr diagram as the measure by which the centre of the circle is displaced from the  $A'_{xx}$  axis. This angle of  $17^\circ$  is a single quantitative measure of the 3D (as opposed to 2D) nature of the CBB tensor.

The concept of a "best 2D strike direction" was introduced above in Section 7 in the context of the Bahr (1988) analysis. Bahr's method, developed for ideal 2D data, may also be applied to 3D data to test whether an "approximate 2D strike direction" is found.

The interpretation approach of CBB is similar. For true 2D data (see the following section) the axes of an ellipse as in Figure 2(b) will be along and across strike; thus for "approximately 2D data" the axes of the ellipse are taken to give an "approximate strike".

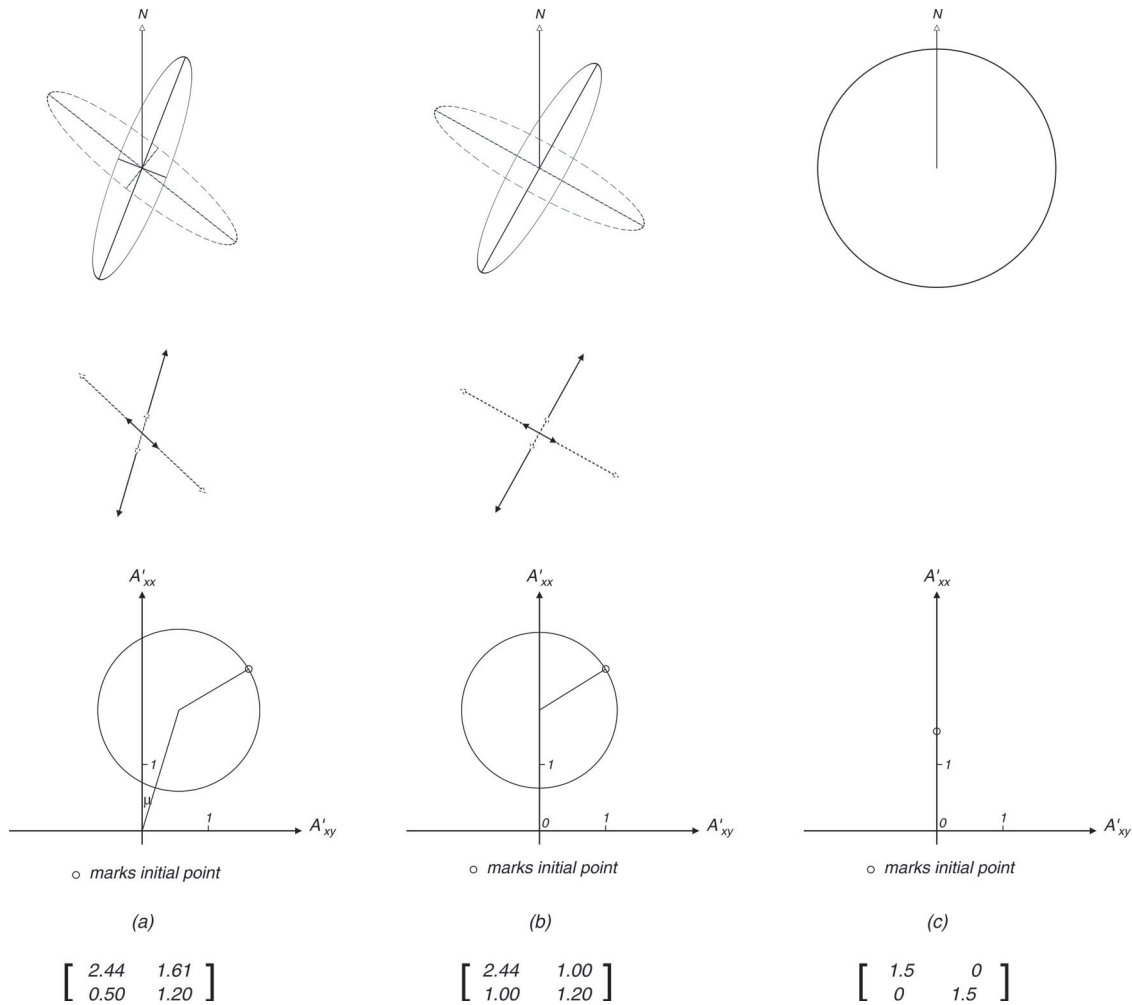


**Figure 7.** Column (a) shows the general 3D case. Column (b) shows the simplifications which occur for 2D. Note that all estimates of strike direction are now the same. Column (c) then shows the further simplifications or characteristics of a 1D case. The concept of geologic strike is no longer relevant. Note that for a uniform half-space, for which the phase is  $\pi/4$  for all orientations of the MT observing axes, the point plotted in (c) would be at the value of unity on the  $A'_{xx}$  axis, because  $\tan \pi/4 = 1$ . Eigenvectors are not given for case (c), as for this case there are no preferred directions (every horizontal direction satisfies the criteria for an eigenvector). Similarly the ellipses have become circles, without any preferred axis directions.

The supplementary ellipse as in Figure 2(a) is relevant here as its axes also, for true 2D data, will be along and across strike. Thus for “approximately 2D data” the axes of this supplementary ellipse also may be taken to give an “approximate strike”. Then, as the axes directions of the two ellipses are different, failing orthogonality by  $17^\circ$  as is evident in column (a) of Figure 7, an indication of a range in the “approximate strike direction” is obtained.

Similarly for true 2D data, the eigenvectors of a CBB tensor lie along and across strike. For 3D data, they may give approximate (but different) 2D strikes, and by their lack of orthogonality (for the current example, the eigenvectors fail orthogonality by  $26.9^\circ$ ) indicate a range in the “approximate strike direction”.

The singular values found,  $w_1$  (3.13) and  $w_2$  (0.679), are taken as estimates of the tangent values of the E-pol and B-pol phases which accompany a 2D model of the 3D data. Similarly, the eigenvalues found  $\zeta_1$  (2.91) and  $\zeta_2$

(0.73) may be taken as estimates of the tangent values of those E-pol and B-pol phases.

**9.2. The 2D case**

Now in Figure 7(b) consider the case  $A = [2.44, 1.00; 1.00, 1.20]$ , which is the 3D tensor depicted in Figure 7(a) artificially modified to give a 2D example.

The two ellipses are orthogonal, demonstrating true 2D structure, and the circle in the Mohr diagram now has its centre on the  $A'_{xx}$  axis. The ellipse axes now show both the 2D strike and its  $90^\circ$  ambiguity, as this strike may be in either of the directions which the ellipse axes indicate.

The points of intersection of the Mohr circle with the  $A'_{xx}$  axis give tangent values of the true E-pol and B-pol phases of the MT data from which the CBB matrix was determined (though the general ambiguity regarding which is which remains). The ellipse axes will be in the ratio of these two tangent values.

Note also that the eigenvectors for the matrix are now orthogonal, in the directions of true 2D strike and across strike. Further note that the eigenvalues also are the true tangent values of the E-pol and B-pol phases of the MT data from which the matrix was notionally determined.

It is this straightforward and useful information given by true 2D cases, concerning E-pol and B-pol phases which may be modelled and especially regarding 2D geologic strike, which encourages the hope that 3D data may be regarded as perturbed 2D data, and approximately correct E-pol, B-pol and strike values found accordingly.

### 9.3. The 1D case of a uniform half-space

Figure 7(c) presents the diagrams for the tensor  $A = [1.5, 0; 0, 1.5]$ , chosen as an ideal 1D case.

The two ellipses take the form of a single circle. There is thus no suggestion of a strike direction, consistent with 1D geological structure.

The Mohr diagram now consists of just a single point, plotted at the 1.5 value on the  $A'_{xx}$  axis.

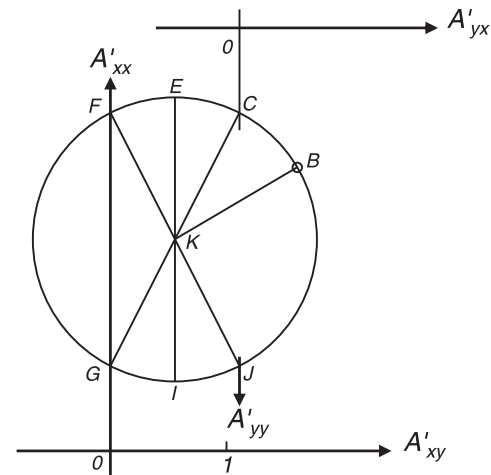
Eigenvectors are not plotted, as the eigenvector condition (Equation (71)) holds for every horizontal direction.

## 10. Interpretation of the SVD results in the context of a choice of maximum and minimum phases

In Figure 5 the arctan of  $w_1$  ( $\arctan 3.13 = 72.3^\circ$  for the current example) is taken as the maximum phase angle, and the arctan of  $w_2$  ( $\arctan 0.679 = 34.2^\circ$  for the current example) is taken as the minimum phase angle. For comparison, it is of interest to see how some other possible values for "maximum" and "minimum" phase plot on such a Mohr diagram. Figure 8 thus extends the discussion of eigenanalysis of the CBB tensor which was begun in Sections 6, 7, 8.2 and Figure 4. The eigenvector points in Figure 4 ( $A'_{yy} = 0.73$  and  $A'_{xx} = 2.91$ ) are marked C and J in Figure 8, and the corresponding eigenvalue points ( $A'_{xx} = 2.91$  and  $A'_{yy} = 0.73$ ) are marked F and G.

Then in Figure 8  $\angle BKC (= 32.6^\circ)$  is twice the rotation of  $16.3^\circ$  (see Section 6 above) to the direction of the first eigenvector, of eigenvalue 2.91. Also reflex  $\angle BKJ (= 266.4^\circ)$  is twice the rotation of  $133.2^\circ$  (as in Section 6) to the direction of the second eigenvector of eigenvalue 0.73.

In Figure 8, the points F and G where the circle cuts the  $A'_{xx}$  axis not only give the eigenvalues, as described. These points also give the values where  $A'_{yy} = 0$ , and so correspond to directions for the  $OY'$  axis when a  $V'_y$  signal gives a  $V'_y$  response only. In this context, the points F and G may be regarded as giving a repeat eigenanalysis, this time using the  $OY'$  direction.



*B* marks initial point

*C* strike direction based on nil  $A'_{yx}$  (a Bahr direction  $\alpha_1 = 16.3$  deg)

*E* strike direction based on maximum  $A'_{xx}$

*F* strike direction based on nil  $A'_{xy}$  (a Bahr direction  $\alpha_3 = 43.2$  deg)

*G* strike direction based on nil  $A'_{xy}$  (a Bahr direction  $\alpha_4 = 106.3$  deg)

*I* strike direction based on minimum  $A'_{xx}$

*J* strike direction based on nil  $A'_{yx}$  (a Bahr direction  $\alpha_2 = 133.2$  deg)

**Figure 8.** Diagram showing various choices for strike direction and maximum and minimum phases, given a CBB matrix with 3D characteristics. On the Mohr circle have been marked the points corresponding to several candidates for "closest 2D strike direction". These are: (i) The Bahr directions which appear as the eigenvector directions, at the points marked C, F, G and J. The corresponding eigenvalues are candidate maximum and minimum phase angles (when their arctangents are taken). (ii) The point E marks the direction of the maximum  $A'_{xx}$  value, which is a candidate for maximum phase value (taking its arctangent). Point E also marks the direction of minimum  $A'_{yy}$  value. (iii) The point I marks the direction of the minimum  $A'_{xx}$  value, which is a candidate for the minimum phase value (taking its arctangent). Point I also marks the direction of maximum  $A'_{yy}$  value.

To rotate the  $OY'$  axis to any particular direction requires a lesser rotation (less by  $90^\circ$ ) than is required to align the  $OX'$  axis to that direction (see Figure 1). Thus the points F and G are (appropriately) diametrically opposite points J and C in Figure 8, the angles  $\angle JKF$  and  $\angle CKG$  of  $180^\circ$  corresponding to rotations of  $90^\circ$ .

Using the notations  $\alpha_1$  and  $\alpha_2$  for the rotation of the  $OX'$  axis to the directions of the first and second eigenvectors respectively,  $\angle CKJ$  is then  $2(\alpha_2 - \alpha_1)$ , and so is a reflex angle of  $233.8^\circ$ . The angle  $\angle CKF$  is then  $2(\alpha_2 - \alpha_1) - \pi$ , of value  $53.8^\circ$ . Angles  $\angle CKE$  and  $\angle EKF$  are thus both  $(\alpha_2 - \alpha_1 - \pi/2)$  and so  $26.9^\circ$ , which is the misfit of the data to Bahr's distorted regional 2D model. Lilley (2018) defines  $\epsilon = \alpha_2 - \alpha_1 - \pi/2$ , and notes that the invariant  $l_7$  of Weaver, Agarwal, and Lilley (2000) is given by  $\sin \epsilon$  (though more correctly  $l_7 = -\sin \epsilon$ ). Weaver, Agarwal, and Lilley (2000) arrive at this estimate in effect via Equations (84) and (89) and their estimate of  $\arcsin l_7$  is  $(\alpha_1 - \alpha_3)$  which in their notation is " $(\theta_1 - \theta_2)$ ". Note that for  $\alpha_2 = \alpha_3 + \pi/2$  as in Figure 3,  $\alpha_1 - \alpha_3 = -\epsilon$ .

Thus the eigenvalues of the CBB tensor are also candidates for “maximum” and “minimum” phase values (taking their arctangents to get actual phase angles), with the eigenvectors (which are also the Bahr directions) being possible “closest” 2D strike directions. The eigenvalue of 2.91 thus gives a maximum phase angle of  $71.0^\circ$ , and the eigenvalue of 0.73 a minimum phase angle of  $36.1^\circ$ .

Further, point E in Figure 8 marks the maximum  $A'_{xx}$  value when the CBB tensor is rotated simply as in Figure 1, without the SVD procedure of two sets of axes rotating separately. Similarly point I marks the point of minimum  $A'_{xx}$ . Thus E and I also give candidate maximum and minimum phase (tangent) values, corresponding to the rotation directions (they will be at right angles) which E and I represent. In terms of the notation of Figure 4 these maximum and minimum phase tangent values will be  $(A_{xx} + A_{yy})/2 + C$  and  $(A_{xx} + A_{yy})/2 - C$  respectively. For the current example, these values are 3.04 and 0.59, giving maximum and minimum phase angles of  $71.8^\circ$  and  $30.6^\circ$  respectively.

Thus in Figure 8, the rotation required (of the axes together as in Figure 1) for  $OX'$  to be in the direction represented by the point E is  $29.8^\circ$  (as angle  $\angle BKE = 59.5^\circ$ ). Similarly, the rotation required for  $OX'$  to be in the direction represented by the point I is  $119.8^\circ$  (as reflex angle  $\angle BKI = 239.5^\circ$ ).

It can be seen that point E in Figure 8 gives a direction which is in effect the arithmetic mean of the two Bahr directions  $\alpha_1$  and  $\alpha_3$  (see Figure 3); while point I gives a direction which is in effect the arithmetic mean of the two Bahr directions  $\alpha_4$  and  $\alpha_2$ .

When the axes are thus rotated, for  $OX'$  to be in the direction represented by the point E, it can be seen that matrix  $A'$  will have the form

$$A' = \begin{bmatrix} (A_{xx} + A_{yy})/2 + C & (A_{xy} - A_{yx})/2 \\ -(A_{xy} - A_{yx})/2 & (A_{xx} + A_{yy}) - C \end{bmatrix} \quad (120)$$

giving the values, for the current numerical example, of

$$A' = \begin{bmatrix} 3.04 & 0.56 \\ -0.56 & 0.59 \end{bmatrix} \quad (121)$$

and emphasising that while the  $A'_{xx}$  element has been maximised (with the value  $3.04 = \tan 71.8^\circ$ ), and the  $A'_{yy}$  element minimised (with the value  $0.59 = \tan 30.6^\circ$ ), the resultant rotated matrix is not diagonal.

## 11. CBB matrices with near-zero and negative determinants

Taking the determinants of both sides of Equation (4) gives

$$\det A = \frac{\det Z_q}{\det Z_p} \quad (122)$$

from which it is immediately seen that  $\det A$  will be positive when  $\det Z_p$  and  $\det Z_q$  are either both positive or

both negative. However,  $\det A$  will be negative when  $\det Z_p$  and  $\det Z_q$  are of opposite sign.

The usual situation is  $\det Z_p$ ,  $\det Z_q$  and  $\det A$  all positive. However other cases occasionally arise perhaps due to error, and flagging negative determinant values may be useful as an error alert.

Quite common is the situation where, especially due to strong local distortion, both  $Z_p$  and  $Z_q$  are near singular, so that their determinants are near zero. In this situation, calculated determinants may be negative, simply due to common error.

Here a fundamental strength of the CBB analysis enters, in that the effects of even near-singular distortion tensors are avoided in Equation (10). Although numerical determinations of  $Z_p$  and  $Z_q$  will involve error, and so in cases of strong distortion it may not be possible to distinguish  $\det Z_p$  and/or  $\det Z_q$  from zero, as long as the distortion tensor does not have a determinant of exactly zero (and in nature such a case is most unlikely) then this determinant cancels out between Equations (4) and (10). The determinant of the distortion tensor is no longer relevant (and remains unknown).

An example is given in Lilley and Weaver (2010, Figs 2 and 4), where the determinant values of the  $Z_p$  and  $Z_q$  data are consistently small (shown in Mohr diagrams by the circles nearly enclosing the axes origins), whereas Mohr diagrams for the CBB matrix data show the circles well clear of the axes origin. In quantitative terms, the condition numbers for the former case are typically 30 and for the latter case are typically 3 (and so an order-of-magnitude less).

In contrast to Equation (122), remembering Equation (10)

$$\det A = \frac{\det Z_q^b}{\det Z_p^b} \quad (123)$$

and the situation now is that  $\det A$  will be positive when  $\det Z_p^b$  and  $\det Z_q^b$  are both positive or both negative. However  $\det A$  will be negative when  $\det Z_p^b$  and  $\det Z_q^b$  are of opposite sign.

Except for negative determinants arising in such cases where strong distortion has affected both  $Z_p$  and  $Z_q$ , observed data with either  $\det Z_p$  negative or  $\det Z_q$  negative are rare. This rarity suggests electromagnetic induction takes place in the Earth in such a way as to generally produce positive  $\det Z_p$  and  $\det Z_q$  values only. Two exceptions are those of the ocean edge observations of Key and Constable (2011), and the continental observations of Selway, Thiel, and Key (2012). It may be significant that in both these cases it is the quadrature part  $\det Z_q$  which is negative; the present author is unaware of any reported cases of negative  $\det Z_p$ .

For cases of negative  $A$  determinants which do arise, analysis of the CBB matrix should be approached with great care, and much of the material of the present paper may be inapplicable. Caldwell, Bibby, and

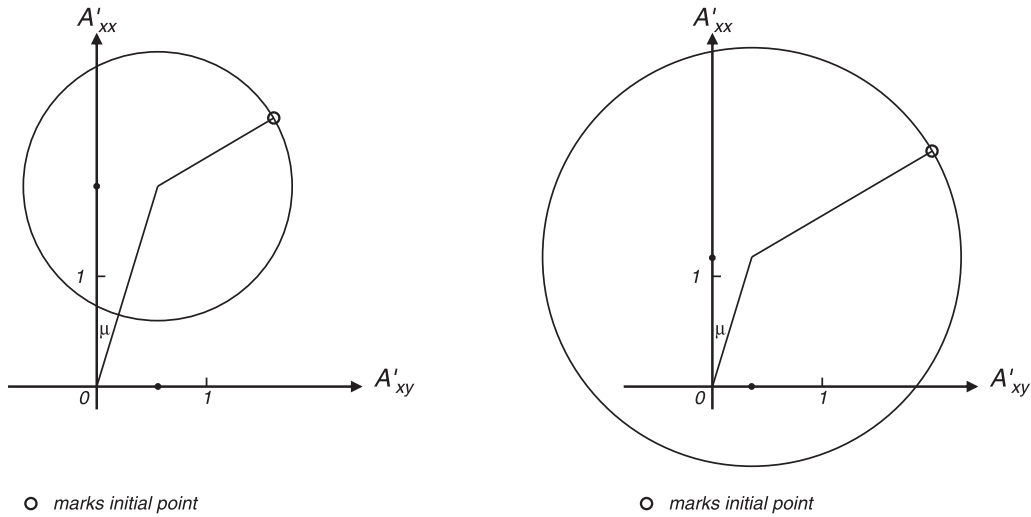


**Figure 9.** The Mohr diagrams for two CBB matrices  $[2.44, 1.61; 0.50, 1.20]$  (left) and  $[2.14, 2.00; 1.28, 0.21]$  (right). The latter has a negative determinant, as shown by the circle enclosing the origin. Both matrices will generate ellipses identical to that shown in Figure 2(b). To distinguish between the two ellipses it is necessary to declare the different signs of their “minimum phase angles” (positive in the first case, negative in the second) or indicate that the ellipses have different directions of rotation, when they are generated by a rotating polar unit vector.

Brown (2004, 469), Bibby, Caldwell, and Brown (2005, 918), Moorkamp (2007) and Caldwell, Bibby, and Brown (2007) all discuss procedures for addressing such negative determinants. Depending on the SVD convention followed, there should be a negative singular value or a reflected direction: this point is discussed in Lilley (2012, 103). If the negative sign is ignored an ellipse will be given, but it will be ambiguous unless a convention is introduced for the sign of ellipse rotation. To illustrate this point, Figure 9 shows the different Mohr diagrams for two different tensors which will both generate the ellipse shown in Figure 2(b).

Regarding eigenvalues, for a negative determinant the circle in a Mohr diagram will enclose the origin of axes, and there will be one negative eigenvalue and one positive eigenvalue (Lilley, 2016, Figure 4).

It should also be noted that when  $\det \mathbf{Z}_p^b$  gets small,  $\det \mathbf{A}$  will get large, and in particular one of the CBB parameters (the singular value  $w_1$ ) will get large, consistent with the large value of the tangent of an angle approaching  $90^\circ$ . Following the procedure of plotting all CBB ellipse axes so that the major axis is of unit length then has the effect of reducing such an ellipse to a line. Indeed it is the infinite range of the tangent function which makes it impracticable, in many instances, to plot the axes of a set of CBB ellipses all to the same scale.

## 12. A comparison of notations used, and some other invariants of the CBB tensor

The quantities  $\theta_1$ ,  $\theta_2$ ,  $\mu$ ,  $w_1$  and  $w_2$  of the present paper are related simply to the quantities  $\alpha$ ,  $\beta$ ,  $\phi_{\min}$  and  $\phi_{\max}$  of Caldwell, Bibby, and Brown (2004), as depicted in Figure 10. Figure 10(c) provides an opportunity to also include the notations  $J_1$ ,  $J_2$  and  $J_3$  of Weaver and

Lilley (2004) which, it can be seen in the figure, are expressed simply in terms of the  $\Phi_1$ ,  $\Phi_2$  and  $\Phi_3$  quantities of Caldwell, Bibby, and Brown (2004). Note that while  $J_1$  and  $J_2$  are positive quantities,  $J_3$  may be positive or negative. Weaver and Lilley (2004) also note that the original CBB tensor can be expressed as

$$\mathbf{A} = J_1 \mathbf{I} + J_2 \mathbf{J} + J_3 \mathbf{K} \quad (124)$$

where  $\mathbf{I} = [1, 0; 0, 1]$ ,  $\mathbf{J} = [\sin \beta, \cos \beta; \cos \beta, -\sin \beta]$  with  $\beta$  as defined by Equation (101) and shown in Figure 4, and  $\mathbf{K} = [0, -1; 1, 0]$ . As can be seen in Figure 10,  $J_1$ ,  $J_2$  and  $J_3$  are gauges for the 1D, 2D and 3D parts respectively of the CBB tensor, and have the values 1.8, 1.2 and 0.56 respectively for the current example.

Figure 10(d) also introduces the notations  $\Pi_1$  and  $\Pi_2$  of Bibby, Caldwell, and Brown (2005). These quantities are respectively the circle radius, and the distance from the origin to the circle centre.

Another invariant relevant in this context is the ratio  $w_1/w_2$ . This ratio is a condition number for the matrix  $\mathbf{A}$ , and is here given the notation  $\kappa_A$ . It has the value 4.6 for the current example. Because it is common to plot CBB ellipses with the major axis of length unity, and the minor axis of length  $w_2/w_1$ , the minor axis thus has a length equal to the reciprocal of the condition number. This length appropriately reduces to zero and the ellipse becomes a straight line in the case of a singular matrix, for which the condition number is infinite.

## 13. Examples of field data

The example given in this section in Figure 11 is the MT data set over its full period range for site NQ101R in Queensland Australia. The matrix  $[2.44, 1.61; 0.50, 1.20]$



NOTATION: THIS PAPER

NOTATION: CBB (2004)

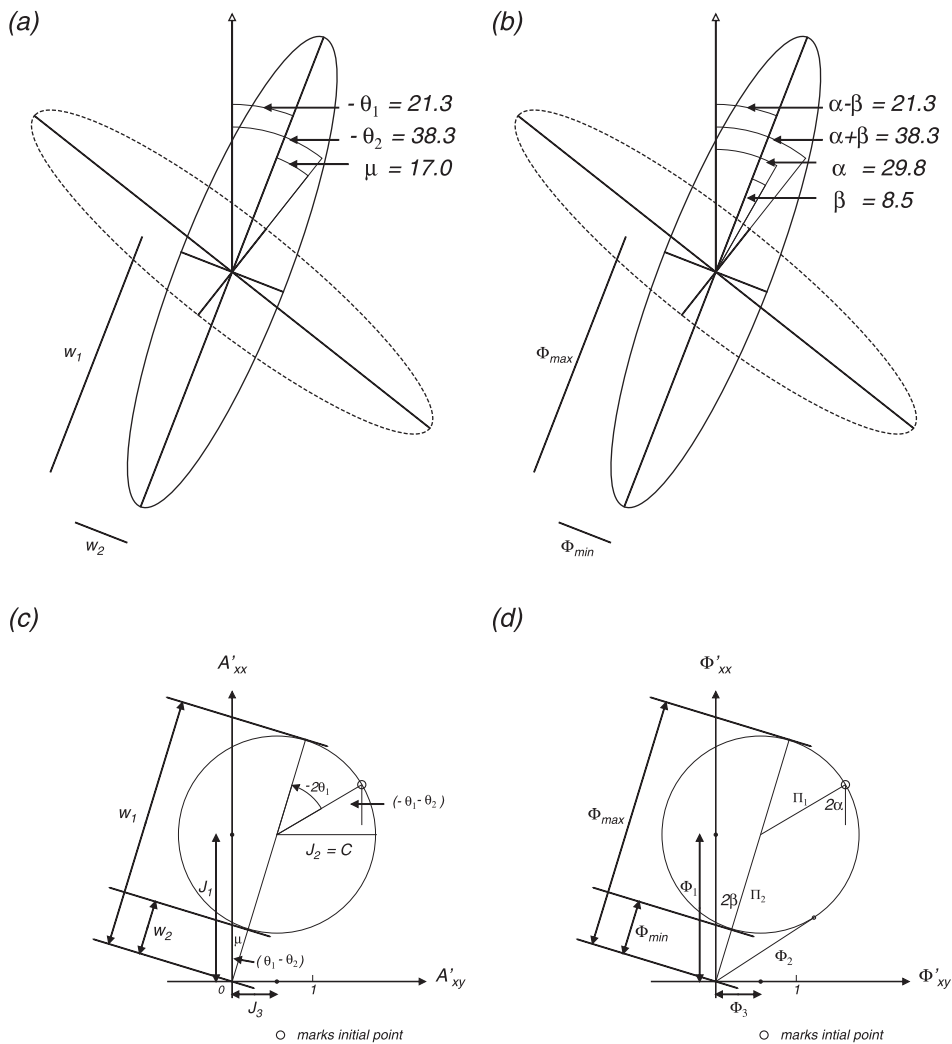


**Figure 10.** Comparison of notations. Left-hand column: Notation as in the present paper. Right-hand column: Notation as in Caldwell, Bibby, and Brown (2004) and see also Heise et al. (2006, Figure 1). Note that the singular values have been drawn to the same scale. For example,  $\Phi_{max}$  in (b), which shows the semi-axis length of the major ellipse, has the same length as  $\Phi_{max}$  in (d), which shows the singular value on the Mohr diagram. Similarly,  $\Phi_{min}$  in (b) has the same length as  $\Phi_{min}$  in (d).

examined in earlier sections of this paper is the  $T = 1.07$  s member of the NQ101R data set.

The data for NQ101R were analysed in the earlier and companion paper (Lilley, 2018) but recently the author was supplied with an amended version of these data (s101R\_edi2.dat). This amended set has formed the basis of the present paper. For completeness and to enable a full comparison with the results of Lilley (2018), amended versions of Figures 7, 8 and 9 of Lilley (2018) are now included here as Figures 12–14.

### 14. Discussion

Figure 11 thus presents the full period-range setting for the numerical example [2.44, 1.61; 0.50, 1.20] which has been used in this paper, and is the NQ101R response for period 1.07s. The elements of matrix  $\mathbf{A}$

are given in panels M1–M2 and N1–N2. The two-dimensionality indicator, angle  $\lambda_A$ , is given in panel M3, and the three-dimensionality indicator, angle  $\mu$ , in panel N3.

Panels M4 and N4 give the “ $\theta_1$  azimuth” and the “ $\theta_2$  azimuth”. These azimuths are based on the  $\theta_1$  and  $\theta_2$  values obtained in Equations (58) and (59). It is first remembered that it is the negatives of these values which give the geographic bearings of the major axes of the ellipses in Figure 2. For the plots in panels M4 and N4 these bearings are then constrained to lie in the first quadrant in the case of  $\theta_1$ , and the second quadrant in the case of  $\theta_2$ , by the addition or subtraction of multiples of  $\pi/2$ . This addition or subtraction of multiples of  $\pi/2$  is allowed by the general ambiguity of not knowing whether a strike direction is along strike or across strike. Thus, for the example matrix [2.44, 1.61; 0.50, 1.20] the

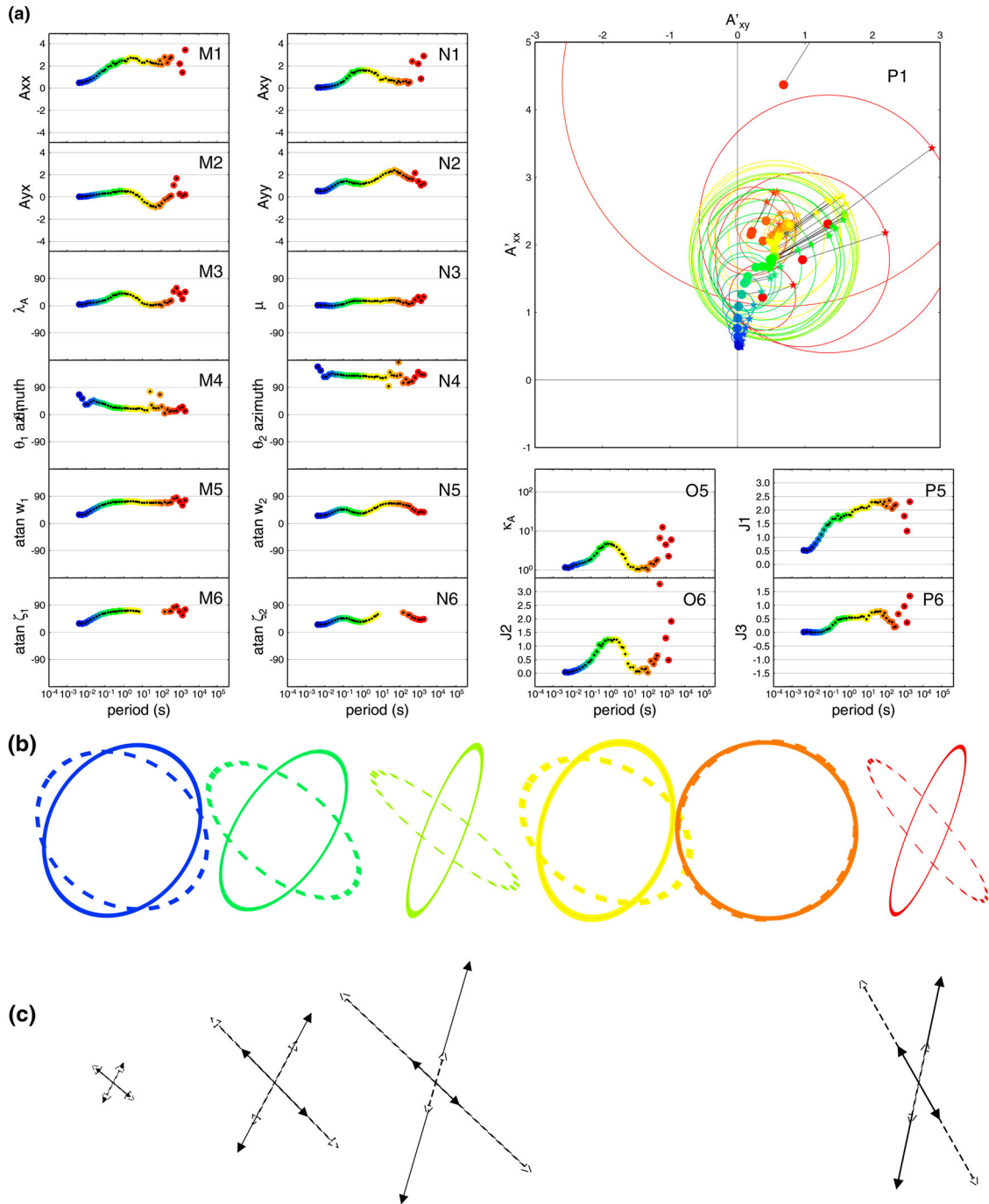


**Figure 11.** (a) The elements of the CBB matrix (panels M1, M2, N1, N2) and their analysis as described in this paper, for station NQ101R (edi2 data). (b) Ellipse pairs representative of periods 0.01 s, 0.1 s, 1 s, 10 s, 100 s and 1000 s, respectively. The same period-dependent colour palette has been used as for part (a). (c) Eigenvectors for the appropriate periods are shown beneath the ellipse pairs to which they apply. Panels M3–M6 and N3–N6 present angles in degrees. All other panels present dimensionless numbers. In (b) and (c)  $T = 1$  s is represented by the  $T = 1.07$  s data, see Figure 2(c,d).

$\theta_1$  value obtained of  $-21.3^\circ$  gives a  $\theta_1$  azimuth of  $21.3^\circ$ , and the  $\theta_2$  value obtained of  $-38.3^\circ$  gives a  $\theta_2$  azimuth of  $128.3^\circ$ .

Panels M5 and N5 give the maximum and minimum phase angles as obtained by SVD (the CBB method), and panels M6 and N6 give the maximum and minimum phase angles obtained by eigenanalysis. Thus M6 is similar to M5, and N6 to N5, except where M6 and N6 have no solutions (in panel P1 the relevant circles do not intersect the vertical axis).

Panel O5 gives the condition number  $w_1/w_2$ , while panels P5, O6 and P6 give the one-, two- and three-dimensionality gauges  $J_1, J_2$  and  $J_3$ , respectively. As would be expected, the general period-dependent behaviour of  $\lambda_A$  in panel M3 is repeated in panels O5 and O6, and that of  $\mu$  in panel N3 is repeated in panel P6.

Panel P1 gives a complete set of Mohr diagrams (with Figure 4 present among them). This panel summarises many of the characteristics of the  $\mathbf{A}$  data.

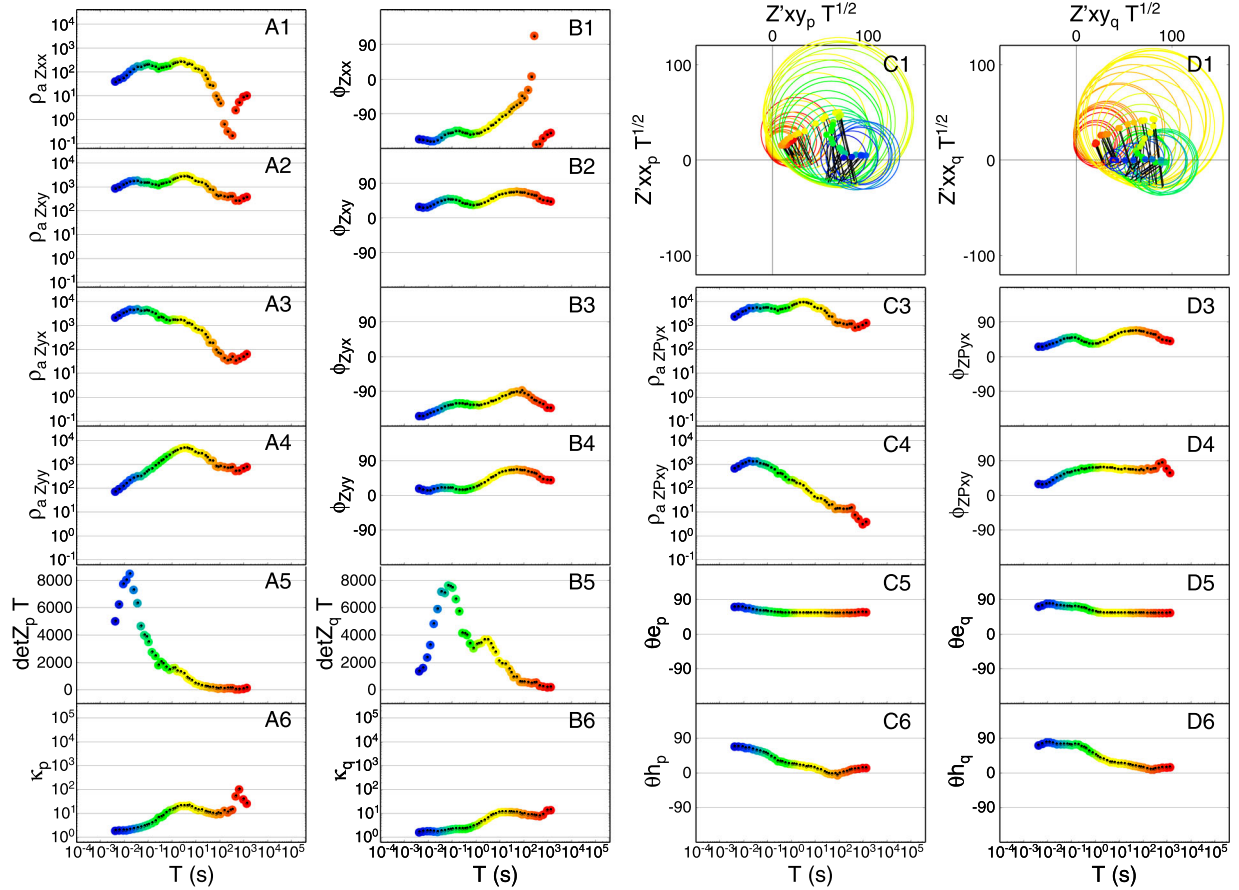


**Figure 12.** Display and analysis by an SVD method of the MT data for the example site NQ101R (edi2 data). The data are closest to 1D at the short period (blue) end of the spectrum, where the “near surface” apparent resistivity is of the order of  $10^3 \Omega\text{m}$ . See text of Lilley (2018) for a description of the results shown. The units for panels A1–A4 and C3–C4 are  $\Omega\text{m}$ , for panels A5 and B5 are  $\text{mV}^2 \cdot \text{km}^{-2} \cdot \text{nT}^{-2} \cdot \text{s}$  and for panels C1 and D1 are  $\text{mV} \cdot \text{km}^{-1} \cdot \text{nT}^{-1} \cdot \text{s}^{1/2}$ . Panels A6 and B6 present dimensionless numbers, and all remaining panels present angles in degrees.

Below the panels are a set of ellipses for a representative range of periods. These ellipses have the form of Figure 2(c), and are coloured according to the palette adopted in the panels above.

Below the ellipses again are sets of eigenvectors for the corresponding periods. As was remarked for panels M6 and N6, eigenvectors are missing where an eigenanalysis of matrix **A** has no solution.

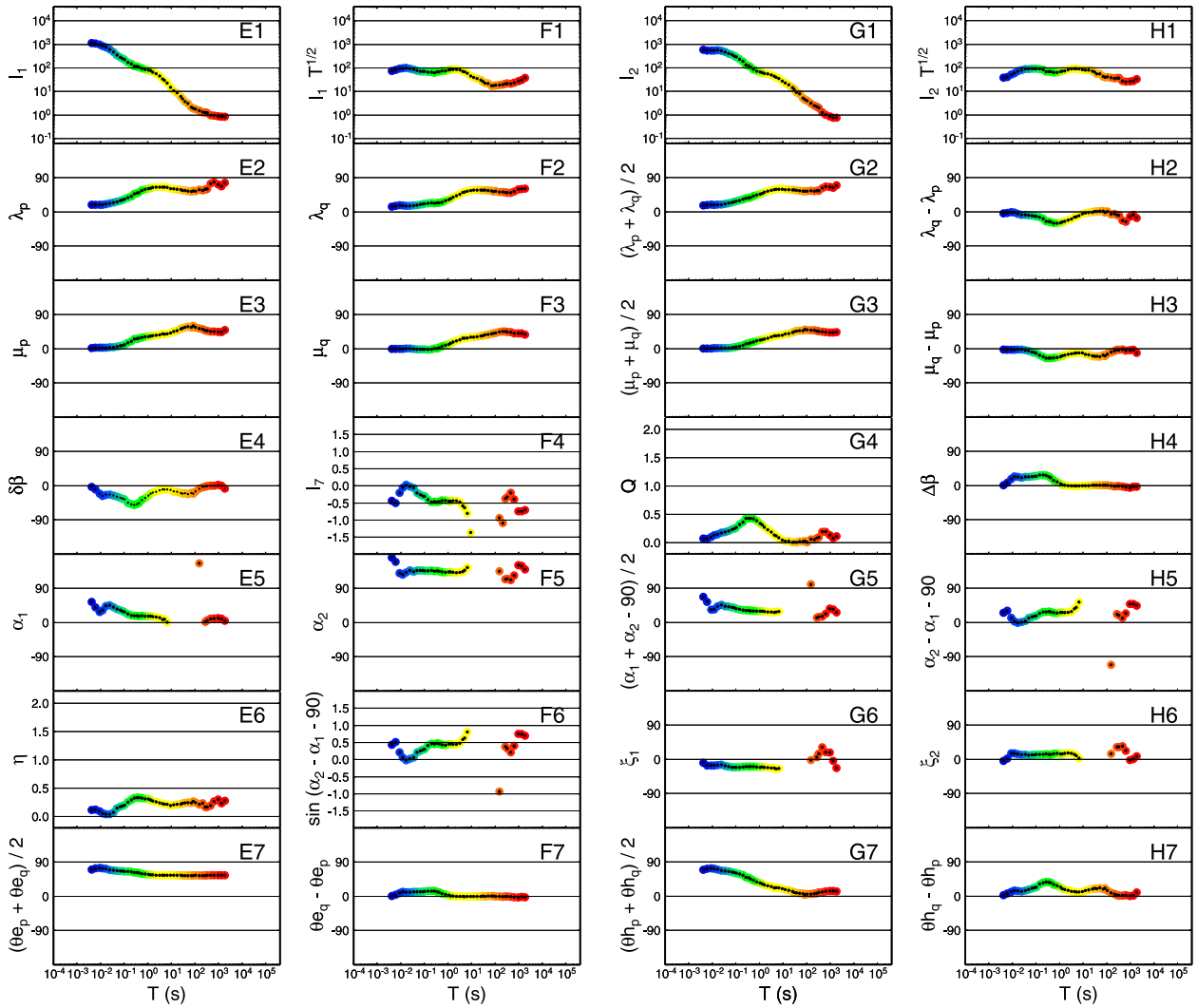
A general summary of the information in Figure 11 is that the data are close to 1D at short periods. With increasing period they become more 2D and 3D, simplifying however to closer to 1D again as the longest periods are reached, at which stage data error causes them to become scattered. A basic model explaining such behaviour is a conductivity structure near the observing site which is not sensed at short periods, but which is part of the MT inductive response at mid-periods. Then at long periods the effects of the structure become purely galvanic, and are removed by the distortion analysis.

Figure 12 shows by the contrast it offers how effective the CBB matrix is in simplifying MT data. For example the complicated phase behaviour seen in panel B1,

and as evident in panel C1 where circles intersect the vertical axis, is now absent from panels M1–M2 and N1–N2 and most notably from panel P1.

Another observation to be made of Figure 12 is the similarity of the phase plots in panels D4 and D3 with the SVD maximum and minimum phase plots in panels M5 and N5 of Figure 11. The phases in panels D4 and D3 result from what may be thought of as SVD analyses of the in-phase and out-of-phase parts of the basic MT tensor separately, see Lilley (2018) and also the earlier papers Lilley (1998a, 1998b). A further study of the theoretical reasons as to why the results in panels D4 and D3 are similar to the results in panels M5 and N5 may prove to be rewarding.

Figure 13, now in review, demonstrates the important point that the Bahr directions  $\alpha_1$  and  $\alpha_2$ , plotted in panels E5 and F5, may be compared with the SVD directions plotted respectively in panels M4 and N4 in Figure 11. The expected similarities are evident except for gaps in panels E5 and F5 where the condition of Bahr (1988) is not met (Lilley, 2018) and, as pointed out in this paper, an eigenanalysis of the CBB matrix has no solution.



**Figure 13.** Analysis of the MT data for site NQ101R (edi2 data) showing values of the invariants as functions of period  $T$ , as described in Lilley (2018). The units for panels E1 and G1 are  $\text{mV}\cdot\text{km}^{-1}\cdot\text{nT}^{-1}$  and for panels F1 and H1 are  $\text{mV}\cdot\text{km}^{-1}\cdot\text{nT}^{-1}\cdot\text{s}^{1/2}$ . Panels E6, F4, F6 and G4 present dimensionless numbers, and the remaining panels present angles in degrees.

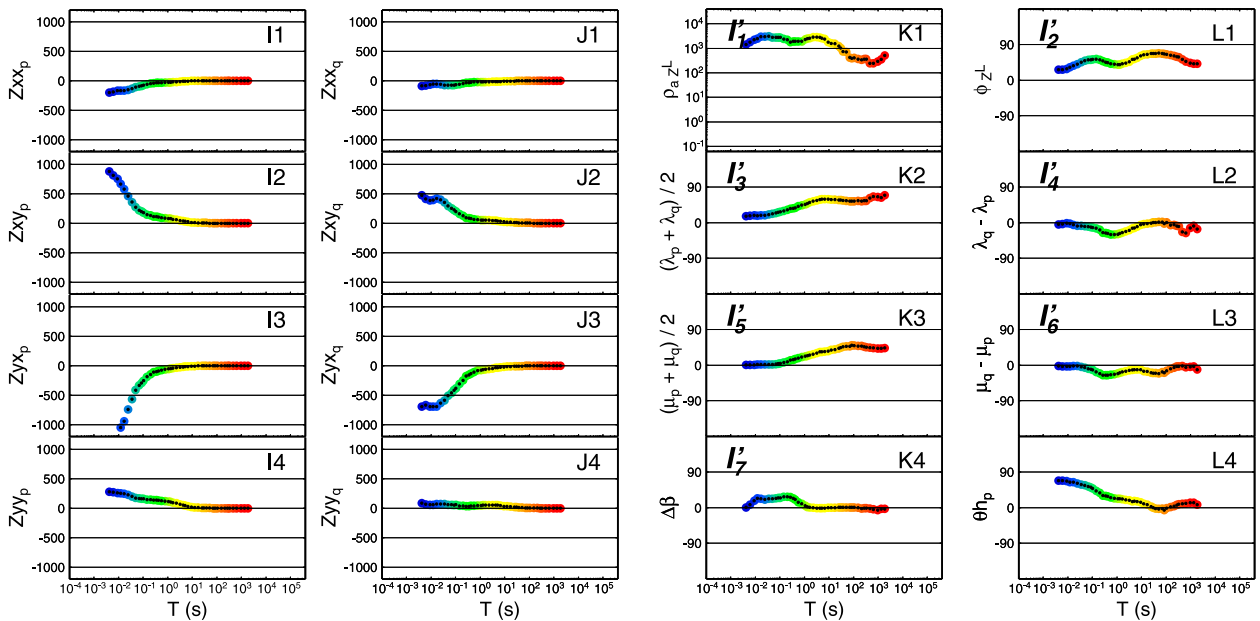


**Figure 14.** Summary of the MT data for site NQ101R (edi2 data), showing on the left the basic tensor elements plotted as functions of period  $T$ , and on the right their representation by the set of invariants,  $l'_1$  to  $l'_7$ , proposed as optimum in Lilley (2018). For panels I1–I4 and J1–J4 the units are  $\text{mV}\cdot\text{km}^{-1}\cdot\text{nT}^{-1}$  and for panel K1 the units are  $\Omega\text{m}$ . The remaining panels present angles in degrees.

## 15. Conclusions

The CBB matrix at the heart of the “phase tensor” may be subjected to various linear algebra techniques such as SVD (Caldwell, Bibby, and Brown, 2004), eigenanalysis, and a simple rotation of axes to maximise and minimise its diagonal elements.

The CBB matrix has a particular value as a dimensionality indicator of the regional geology, and the ellipses from SVD show this information clearly, especially when plotted as a pair. Mohr diagrams also show dimensionality information clearly, as do plots of the eigenvectors of a CBB matrix.

The inverse of the CBB matrix holds similar information to the CBB matrix itself. Ellipses from the SVD analysis of this inverse, and vectors from its eigenanalysis, supplement the information from the basic CBB matrix in a useful way.

It is a common current practice to compute a CBB matrix, and immediately represent it as a single ellipse. A major theme of the present paper is to emphasise the distinction between these two steps, of computation and diagrammatic representation. Having taken the first step, this paper points out that there may be value in pausing and looking more widely before taking the second step. The eigenanalysis of a CBB matrix may yield useful information, as may the simple rotation of the matrix to maximise and minimise its diagonal elements. Further the results from analysing the matrix inverse may also yield useful information.

## Acknowledgements

The author thanks many colleagues who have contributed ideas and discussion to the material described in this paper, especially Chris Phillips and John Weaver. Peter Milligan, a friend and colleague who died in March 2019 while the paper was in preparation, was the source of much information and many stimulating conversations on magnetotelluric matters. Interaction with Peter was greatly valued and is sadly missed. Comments by Sahereh Aivazpourporgou and an anonymous reviewer have proved very helpful and are much appreciated. Mark Lackie and Graham Heinson are thanked for editorial support. The software of Wessel and Smith (1998) has been used to produce the figures of this paper.

## Disclosure statement

No potential conflict of interest was reported by the author.

## ORCID

Frederick E. M. Lilley  <http://orcid.org/0000-0003-3785-3704>

## References

Avdeeva A., Moorkamp M., Avdeev D., Jegen M., and Miensoopust M. 2015. Three-dimensional inversion of magnetotelluric impedance tensor data and full distortion matrix. *Geophysical Journal International* 202: 464–81.

- Bahr K. 1988. Interpretation of the magnetotelluric impedance tensor: Regional induction and local telluric distortion. *Journal of Geophysics* 62: 119–27.
- Bibby H.M. 1986. Analysis of multi-source bipole-quadrupole resistivity surveys using the apparent resistivity tensor. *Geophysics* 51: 972–83.
- Bibby H.M., Caldwell T.G., and Brown C. 2005. Determinable and non-determinable parameters of galvanic distortion in magnetotellurics. *Geophysical Journal International* 163: 915–30.
- Booker J.R. 2014. The magnetotelluric phase tensor: A critical review. *Surveys in Geophysics* 35: 7–40.
- Caldwell T.G., Bibby H.M., and Brown C. 2004. The magnetotelluric phase tensor. *Geophysical Journal International* 158: 457–69.
- Caldwell T.G., Bibby H.M., and Brown C. 2007. Comment on “The magnetotelluric phase tensor” by T. Grant Caldwell, Hugh M. Bibby and Colin Brown – reply. *Geophysical Journal International* 171: 567.
- Chave A.D., and Jones A.G., eds. 2012. *The magnetotelluric method: Theory and practice*. Cambridge: Cambridge University Press.
- Frazer R.A., Duncan W.J., and Collar A.R. 1963. *Elementary matrices*. Cambridge: Cambridge University Press.
- Heise W., Caldwell T.G., Bibby H.M., and Brown C. 2006. Anisotropy and phase splits in magnetotellurics. *Physics of the Earth and Planetary Interiors* 158: 107–21.
- Kelbert A., Meqbel N., Egbert G.D., and Tandon K. 2014. ModEM: A modular system for inversion of electromagnetic geophysical data. *Computers and Geosciences* 66: 40–53.
- Key K., and Constable S. 2011. Coast effect distortion of marine magnetotelluric data: Insights from a pilot study offshore northeastern Japan. *Physics of the Earth and Planetary Interiors* 184: 194–207.
- Lilley F.E.M. 1976. Diagrams for magnetotelluric data. *Geophysics* 41: 766–70.
- Lilley F.E.M. 1998a. Magnetotelluric tensor decomposition: Part I, Theory for a basic procedure. *Geophysics* 63: 1885–97.
- Lilley F.E.M. 1998b. Magnetotelluric tensor decomposition: Part II, Examples of a basic procedure. *Geophysics* 63: 1898–1907.
- Lilley F.E.M. 2012. Magnetotelluric tensor decomposition: Insights from linear algebra and Mohr diagrams. In *New achievements in geoscience*, ed. H.S. Lim, chap. 4, 81–106. London: InTech Open Science.
- Lilley F.E.M. 2016. The distortion tensor of magnetotellurics: A tutorial on some properties. *Exploration Geophysics* 47, no. 2: 85–99.
- Lilley F.E.M. 2018. The magnetotelluric tensor: Improved invariants for its decomposition, especially ‘the 7th’. *Exploration Geophysics* 49: 622–36.
- Lilley F.E.M., and Phillips C.J.E. 2018. A property of the determinant of a  $2 \times 2$  tensor relevant to magnetotellurics. *Geophysics* 83: A59–A64.
- Lilley F.E.M., and Weaver J.T. 2010. Phases greater than  $90^\circ$  in MT data: Analysis using dimensionality tools. *Journal of Applied Geophysics* 70: 9–16.
- Moorkamp M. 2007. Comment on “The magnetotelluric phase tensor” by T. Grant Caldwell, Hugh M. Bibby and Colin Brown. *Geophysical Journal International* 171: 565–6.
- Nye J.F. 1957. *Physical properties of crystals*. Oxford: Oxford University Press.
- Robertson K.E., Heinson G.S., Taylor D.H., and Thiel S. 2017. The lithospheric transition between the Delamerian and Lachlan orogens in western Victoria: New insights from 3D magnetotelluric imaging. *Australian Journal of Earth Sciences* 64: 385–99.

- Selway K., Thiel S., and Key K. 2012. A simple 2-D explanation for negative phases in TE magnetotelluric data. *Geophysical Journal International* 188: 945–58.
- Strang G. 2006. *Linear algebra and its applications*. 4th ed. San Francisco: Cengage–Brooks/Cole.
- Tietze K., Ritter O., and Egbert G.D. 2015. 3-D joint inversion of the magnetotelluric phase tensor and vertical magnetic transfer functions. *Geophysical Journal International* 203: 1128–48.
- Weaver J.T., and Lilley F.E.M. 2004. Using Mohr Circles to identify regional dimensionality and strike angle from distorted magnetotelluric data. *Exploration Geophysics* 35: 251–4.
- Weaver J.T., Agarwal A.K., and Lilley F.E.M. 2000. Characterization of the magnetotelluric tensor in terms of its invariants. *Geophysical Journal International* 141: 321–36.
- Weaver J.T., Agarwal A.K., and Lilley F.E.M. 2003. The relationship between the magnetotelluric tensor invariants and the phase tensor of Caldwell, Bibby and Brown. In *Three-dimensional electromagnetics III*, ed. J. Macnae and G. Liu, no. 43 in Paper, 1–8. Sydney: ASEG.
- Weaver J.T., Agarwal A.K., and Lilley F.E.M. 2006. The relationship between the magnetotelluric tensor invariants and the phase tensor of Caldwell, Bibby and Brown. *Exploration Geophysics* 37: 261–7.
- Weidelt P., and Chave A.D. 2012. The magnetotelluric response function. In *The magnetotelluric method: Theory and practice*, ed. A.D. Chave and A.G. Jones, 122–164. Cambridge: Cambridge University Press.
- Wessel P., and Smith W.H.F. 1998. New, improved version of generic mapping tools released. *Eos, Transactions American Geophysical Union* 79: 579.